Privatdoz. Sven Barth

TU WIEN TECHNISCHE UNIVERSITÄT WIEN

DIPLOMARBEIT

Nucleation and Growth of Metastable Ge$_{1-x}$Sn$_x$ Alloy Nanowires with High Tin Content

Ausgeführt am Institut für

Materialchemie

der Technischen Universität Wien

unter der Anleitung von

Privatdoz. Dipl.-Chem. Dr.rer.nat. Sven Barth

durch

Michael Stanislaus Seifner, BSc.

Kirchberg 12, 7453 Steinberg-Dörfl

Wien, Juni 2016

Michael S. Seifner, BSc.

"I don't know where I'm going from here, but I promise it won't be boring"

David Bowie

Statutory Declaration

I herewith declare that I have authored this thesis independently, that I have not used other than the declared sources/resources, and that I have explicitly marked all material which has been quoted either literally or by content from the used sources.

Eidesstattliche Erklärung

Ich erkläre hiermit an Eides statt, dass ich die vorliegende Diplomarbeit selbstständig und ohne fremde Hilfe verfasst, andere als die angegebenen Quellen und Hilfsmittel nicht benutzt und die den benutzten Quellen wörtlich und inhaltlich entnommenen Stellen als solche erkenntlich gemacht habe.

Parts of this thesis have been published

- S. Barth, M. S. Seifner, J. Bernardi, *Chemical Communications* **2015,** *51*, 12282-12285.

- M. S. Seifner, F. Biegger, A. Lugstein, J. Bernardi, S. Barth, *Chemistry of Materials* **2015,** *27*, 6125-6130.

- S. Barth, M. S. Seifner, *Nachrichten aus der Chemie* **2015,** *63*, 1172-1175.

Acknowledgement

At this point I would like to thank…

…Sven for showing me that with a good idea many things are possible, spending his time to answer many of my questions, acquiring SEM as well as TEM images and training me in a positive way.

…Marlene for being my life companion and giving me a smile every day.

…my mother Andrea for always giving an ear to me in tough times, fostering my interests early on and making me the person I am.

…my father Gerald for reminding me not to forget all the important things in life and letting me win in billiards all the time.

…my sister Franziska for being a great friend and accompanying me since she was born.

…my family, that I love to be part of, for the unconditional support and the great experiences we share.

…my friends for their support and the time we spend together.

…my former chemistry teacher Michael for drawing my interest in chemistry.

…Felix for being a great colleague and a helpful person, sharing funny moments together and always giving an ear to me.

…Patrik for the interesting discussions about our research topic and the good collaboration.

…Lukas for putting the whole group into good humour.

…the whole institute for the friendly working atmosphere.

…the "Universitäre Service-Einrichtung für Transmissions-Elektronenmikroskopie" of the Vienna University of Technology for access to the SEM and TEM facilities.

…the Vienna University of Technology X-ray center for access to the XRD facilities.

…A. Lugstein and Y. Hosseinnia for the µ-Raman measurements.

Abstract

The first bottom-up synthesis procedure for $Ge_{1-x}Sn_x$ nanowires with a high tin content of 12.4 ± 0.6 % and constant diameter along their axis was developed. The synthesis was enabled by using a microwave approach in combination with metalorganic precursors. The keys to success have been attributed to the ratio of homo- and heterometallic derivatives in the precursor mixture, the pretreatment of the precursor mixture and the low temperatures used for the synthesis. The different morphologies of the synthesised nanowires pointed towards the specific growth regimes, which were related to the decomposition of the homo- and heterometallic precursor species providing germanium and tin for the $Ge_{1-x}Sn_x$ growth. Based on these results, a modified procedure was developed for the controlled growth of $Ge_{1-x}Sn_x$ nanowires with constant diameter and a high tin content.

EDX elemental mapping images confirmed the homogenous distribution of tin in the germanium lattice, while HRTEM images show the high crystallinity of the $Ge_{1-x}Sn_x$ nanowires. Independent and complementary techniques, such as XRD, Raman and EDX analysis have been performed for the determination of the tin content. HRTEM images suggest the appearance of oriented attachment during the nucleation regime of $Ge_{1-x}Sn_x$ nanowires with constant diameter. Furthermore, $Ge_{1-x}Sn_x$ nanowires with diminishing diameter showed an increasing amount of tin incorporated into the germanium lattice towards the tip area. The increased percentage of tin can be related to the smaller diameter of the materials and thus a more effective strain release accompanied with a higher amount of tin in the germanium lattice. These results represent important findings for the controlled synthesis of nanoscale, metastable $Ge_{1-x}Sn_x$.

Kurzfassung

In dieser Arbeit wird das erste Bottom-up-Verfahren zur Herstellung von $Ge_{1-x}Sn_x$ Nanodrähten mit einem hohen Zinngehalt von 12.4 ± 0.6 % und konstantem Durchmesser entlang der Wachstumsachse vorgestellt. Die erfolgreiche Synthese basiert auf molekularen Vorstufen, die in einem Mikrowellenprozess thermisch zersetzt werden. Der Schlüssel zum Erfolg wird dem Verhältnis der auftretenden Intermediaten in der Mischung, der Vorbehandlung dieser Vorstufenmischung und den vergleichsweise geringen Temperaturen während der Synthese zugeschrieben. Die unterschiedlichen Strukturen der synthetisierten Nanodrähte legen das Auftreten verschiedener Wachstumsregime nahe, welche der Zersetzung unterschiedlicher homo- und heterometallischen Vorstufen, und der damit verbundenen Festlegung des Germanium-Zinn-Verhältnisses, zugeschrieben werden können. Diese Erkenntnisse machen ein kontrolliertes Wachstum von $Ge_{1-x}Sn_x$ Nanodrähten mit konstantem Durchmesser und einem hohen Zinngehalt möglich.

EDX-Elementverteilungsmessungen zeigen eine gleichmäßige Verteilung von Zinn im Germaniumgitter, während HRTEM-Bilder die hohe Kristallinität der Nanodrähte bestätigen. Zur Bestimmung des Zinngehalts wurden komplementäre XRD-, Raman- und EDX-Messungen durchgeführt. HRTEM-Bilder legen eine orientierte Anlagerung während des Nukleationregimes der $Ge_{1-x}Sn_x$ Nanodrähte mit konstantem Durchmesser nahe. Außerdem konnte gezeigt werden, dass bei $Ge_{1-x}Sn_x$ Nanodrähte mit abnehmendem Durchmesser in Richtung der Spitze des Nanodrahtes mehr Zinn in das Germaniumgitter eingebaut werden kann. Der höhere Zinngehalt kann auf einen effektiveren Abbau von Verspannungen über die Oberfläche des Nanodrahtes mit geringerem Durchmesser erklärt werden. Diese Ergebnisse liefern sehr wichtige Erkenntnisse, die zur kontrollierten Synthese von nanoskaligem, metastabilem $Ge_{1-x}Sn_x$ verwendet werden können.

Table of Contents

1 Introduction

Nowadays a wide range of materials with specific properties is available and well-known. The main challenges are associated with a controlled synthesis of materials in terms of structure and properties to improve existing devices and to foster these specific properties for new applications.

In the area of semiconductor materials, group 14 elements (Si, Ge) and alloys ($Si_{1-x}Ge_x$, $Ge_{1-x}Sn_x$) have high potential to be applicable in silicon based devices due to their good compatibility with the established processing techniques. The main disadvantage of thermodynamically stable group 14 semiconductors at atmospheric conditions is the low efficiency of emission due to the indirect band gap behaviour. The optical and electronic properties of group 14 semiconductors can be strongly influenced by compressive and tensile strain leading to band bending and an associated transition from an indirect to a direct band gap semiconductor.[1] For this purpose, the epitaxial relation between the substrate and the active material is very important for semiconductor engineering in thin film processes.

The transition to a direct band gap material can also be achieved by composition tuning. Based on theoretical studies, group 14 alloys of certain compositions are direct band gap materials.[1-3] However, with the exception of the Ge/Si-system, the solid solubility of a heavier homologue in the silicon or germanium lattice is very low due to the large mismatch of atomic radii. The required composition of these group 14 alloys leading to a direct band gap is typically in the metastable range. For this reason the synthesis of these alloys has to be performed under kinetic and not thermodynamic control.[4-5]

The main advantage of group 14 semiconductors compared to other promising materials like III-V-semiconductors, which have similar applications, is the possibility of simple implementation in already existing processes based on silicon[4] and the biocompatibility of the material[6]. This thesis will give a short overview of semiconductors used for optical and electronic devices and will focus on the synthesis of metastable group 14 alloys via kinetically controlled processes without the use of a templating surface.

2 Theoretical part

2.1 Group 14 semiconductors

Elements and alloys of the group 14, containing C, Si, Ge, Sn and Pb, are discussed in this chapter. To understand their special properties and the trends within the group, some facts are presented in table 1.

Table 1: Summary of some important properties of group 14 semiconductor crystals with the diamond structure.[7]

Element	Phase stability at ambient conditions	Lattice constant of the diamond cubic crystal structure [Å]	Band gap [eV] (at 300 K)
C	metastable	3.567	5.48
Si	stable	5.431	1.12
Ge	stable	5.658	0.66
Sn	metastable	6.489	0.08

Each element of the group 14 has a large number of allotropes. For instance, carbon allotropes include diamond (cubic), graphite, lonsdaleite (hexagonal diamond), fullerenes, *etc.*[8] Under standard conditions silicon is thermodynamically stable in the diamond structure, while the hexagonal diamond structure is metastable. Hexagonal silicon has the advantage of being a direct band gap material, but the synthesis of reasonable quantities remained challenging. Recently, a rational synthesis procedure for the synthesis of hexagonal silicon using appropriate substrates has been reported.[9]

Germanium is stable in the diamond structure (α-germanium) under standard conditions. In addition, the tetragonal (β-germanium) and the hexagonal form of germanium are known.[10-11] Analogous to the hexagonal silicon, the hexagonal germanium has the benefit of being a direct band gap material. Tin is very similar to germanium with the difference that the metallic tetragonal form (β-tin) is the stable allotrope at standard conditions. The diamond structure of tin (α-tin) is a zero band gap semiconductor and stable at slightly lower temperatures.[12]

Compared to the other group 14 elements, lead has a small number of allotropes. The most common is the face-centered cubic form, which has metallic properties and is therefore not important for the semiconductor industry. Besides this fact, lead is also toxic, which is not the case for the other elements of group 14.

Nowadays, many optical and electronic devices are based on cubic silicon. Therefore, new materials are easier implemented in existing processes of the semiconductor industry when the materials can be grown epitaxially on these silicon substrates. Epitaxial films of cubic germanium can be grown on silicon single crystals. The lattice mismatch between silicon and germanium leads to an induction of compressive strain in the germanium layer, which is changing the band structure of cubic germanium. The germanium lattice is able to relax for higher film thicknesses and has the same properties as the bulk material. Strain related effects on the properties are discussed in detail below.

The latest development is the improvement of pure group 14 semiconductors by alloying them with other group 14 elements. This is not trivial, because except of the Si/Ge-phase diagram, the binary phase diagrams of theoretically promising alloys show a low solubility of group 14 elements in each other (figure 1).[13] According to theoretical and experimental studies, the content of the alloying element of the promising materials is often far above the thermodynamic solubility limit and is therefore a metastable alloy. In the case of $Ge_{1-x}Sn_x$ 6.5-11 % of tin is needed to convert the cubic germanium from an indirect into a direct band gap material.[1-2,14] There is also a single theoretical study which predicts a direct band gap behaviour for $Ge_{1-x}Pb_x$ for 1 % of lead.[3] In both cases the interesting composition is not within the thermodynamically stable range as shown in figure 2b for $Ge_{1-x}Sn_x$ with a solid solubility of ~1.1 % tin. The most promising material for the improvement of optical

and electronic devices in the recent years is $Ge_{1-x}Sn_x$.[14-15] Therefore, this section is focusing on the properties and synthesis of the Ge-Sn alloy.
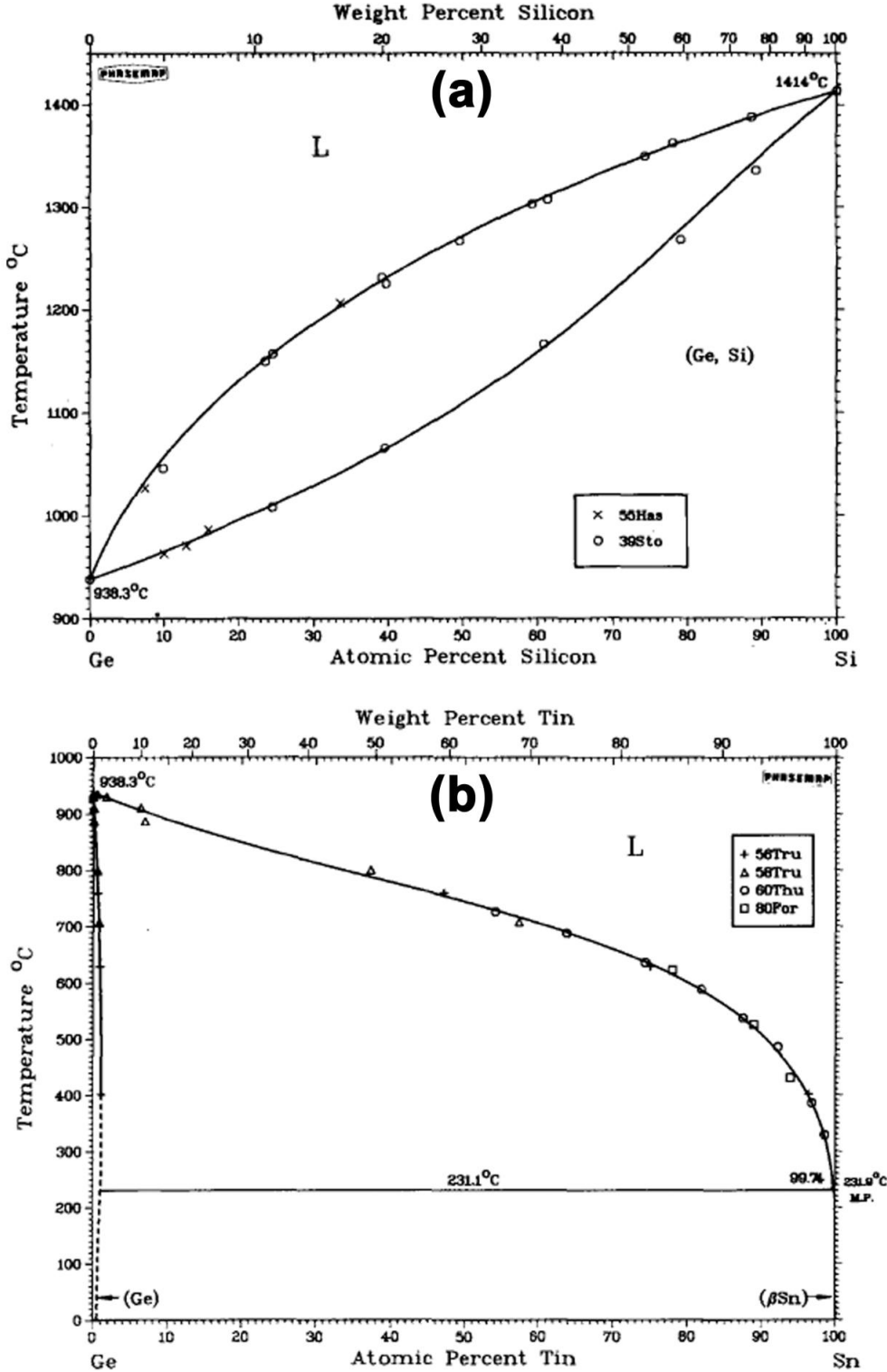
Figure 1: Binary phase diagrams of (a) Ge/Si[13] and (b) Ge/Sn[16]. Reproduced with permissions from Springer.[13,16]

It is very important to understand the band structure of pure cubic germanium and to recognise changes upon straining of cubic germanium or alloying with tin for the potential improvement of the optical and electronic properties.
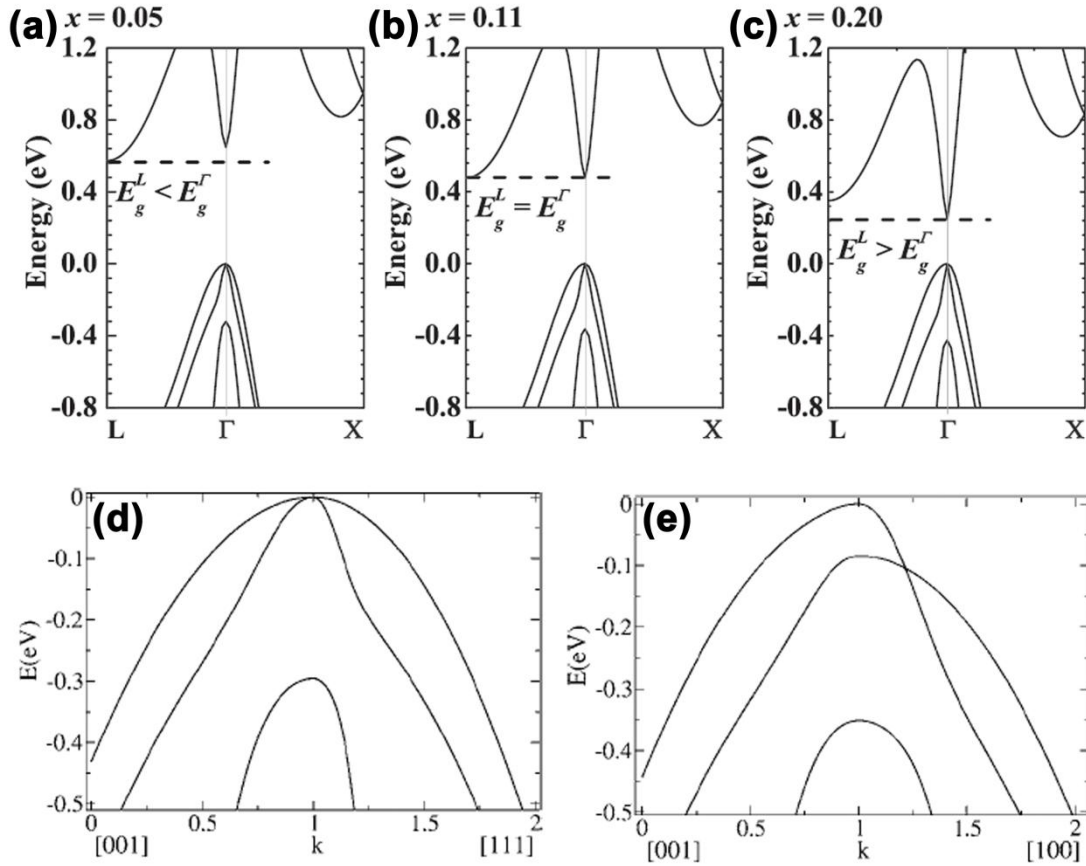
Figure 2: Electronic band structure of $Ge_{1-x}Sn_x$ along L-Γ-X for (a) $x = 0.05$, (b) $x = 0.11$, and (c) $x = 0.20$.[2] (d) shows the valence band structure of unstrained Ge along [001]-Γ-[111] and (e) shows the valence band maximum structure of [100] strained Ge zoomed in around Γ.[17] Reproduced with permissions from AIP Publishing LLC[2] and the American Physical Society[17].

First the role of inducing strain is neglected, but it is obvious that this assumption is not always valid for thin films grown on a substrate. Therefore, the assumption in this case is that the material has a high surface-to-volume ratio[18-19] or the epitaxially grown layer is very thick, which allows the structure to relax[20].

Pure germanium is an indirect band gap material due to the required change of momentum for a transition from the valence to the conduction band. This requirement results in a very low efficiency of the transition and makes the application as an optical material problematic. To increase the efficiency, the conversion to a direct band gap material is necessary. As stated above, the transition can be achieved by lowering the direct band gap in respect to the indirect band gap (figure 2a-c). The direct band gap is shrinking much more with increasing tin content in $Ge_{1-x}Sn_x$ than the indirect band. The threshold concentration is reported to be in the range of 6.5-11 % of tin with the most reliable sources reporting the higher values.[1-2,14] In addition, the tin atoms have to be at substitution sides in the lattice to achieve this effect.[21-23] With increasing tin content, the germanium lattice is expanding. This effect can be described by the Vegard's law, which predicts a linear dependence of the lattice parameter on the concentration of the alloying element in solid solutions.[24] It depends on several factors, whether the use of the Vegard's law is valid for metallic alloys or not.[25-27] In the case of the $Ge_{1-x}Sn_x$ alloy, Vegard's law can be applied but must be modified by the bowing parameter due to a slight overestimation of the tin content by the calculations. The latest advances concerning the experimental determination of the bowing parameter are in good agreement with theoretical results.[20,28]

$$a_{GeSn} = a_{Ge} \cdot (1-x) + a_{Sn} \cdot x + b \cdot x \cdot (1-x)$$

$$a_{GeSn} = \text{lattice constant of } Ge_{1-x}Sn_x \text{ [Å]}$$
$$a_{Ge} = \text{lattice constant of Ge [Å]}$$
$$a_{Sn} = \text{lattice constant of Sn [Å]}$$
$$x = \text{mole fraction of Sn [ ]}$$
$$b = \text{bowing parameter [Å]}$$

Equation 1: Vegard's law modified by a bowing parameter.[20]

As already mentioned before, the band gap is lowered by alloying germanium with tin which allows the band gap tuning by controlling the tin content. The band gap of the $Ge_{1-x}Sn_x$ alloy with *x* near the transition point has a value of about 0.477 eV, which is equal to radiation in the near-IR range.[2] Increasing the tin content leads to further reduction of the band gap shifting absorption and emission wavelengths in the mid-IR range. This radiation is used in medical diagnostics due to the low absorption of mid-IR radiation by the human body and can be detected by implementing $Ge_{1-x}Sn_x$ on a chip to build a photonic device. In addition, lasers in the mid-IR region would also be interesting devices for high-speed communications.[29]

In this research area group 14 alloys are competing with III-V-semiconductors. III-V-semiconductors are prime examples, when talking about photonic devices due to their direct band gap behaviour. The main challenge in this research area is the implementation of III-V-semiconductors on silicon based devices compared to pure group 14 photonics, although some interesting approaches exist already to achieve this goal.[19,30-31] Some aspects about the III-V-/IV-IV-semiconductor topic and the opportunities and challenges of group 14 photonics have been discussed by Richard Soref.[32]

In thin film techniques $Ge_{1-x}Sn_x$ alloys are grown on silicon or on virtual germanium substrates (figure 3a + b + d).[4] For thin $Ge_{1-x}Sn_x$ layers the lattice mismatch of the involved materials cannot be fully compensated leading to an induction of strain in the grown layer. The relaxation of the strained $Ge_{1-x}Sn_x$ lattice is associated with the formation of defects, such as dislocations at the interface (figure 3c).[20] In most cases these defects are not beneficial for the materials properties, because the dislocations can act as recombination centres leading to quenching of the emission.[33] Strain effects are responsible for the inability to grow direct band gap $Ge_{1-x}Sn_x$ on virtual germanium substrates due to the induction of compressive strain, which counteracts the expansion of the crystal lattice by alloying with tin.[34]
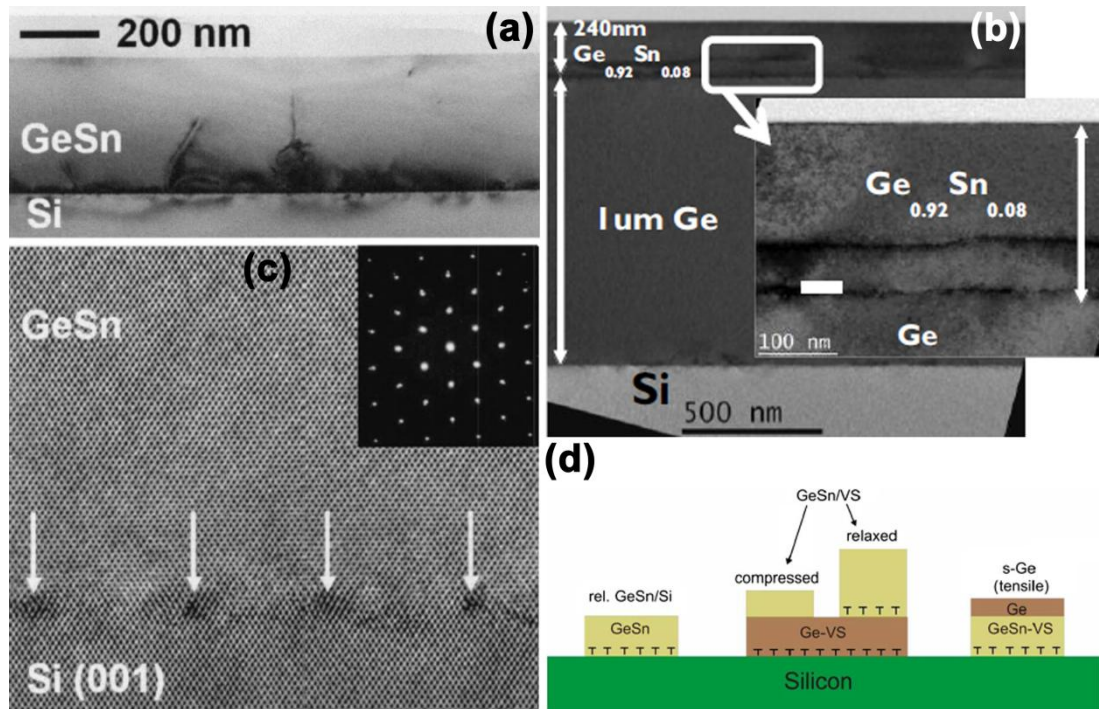
Figure 3: Cross-sectional transmission electron microscopy (XTEM) images show the thin film growth of (a) $Ge_{1-x}Sn_x$ directly on silicon[21] and (b) on a virtual germanium substrate[20]. The high-resolution transmission electron microscopy (HRTEM) image in (c) shows the relaxation of the $Ge_{1-x}Sn_x$ layer above a critical thickness which leads to the appearance of dislocations.[21] (d) Possible substrate strategies for producing photonic devices on silicon.[4] Reproduced with permissions from AIP Publishing LLC[21], the Electrochemical Society[20] and OSA Publishing[4].

In addition to the changes in the band gap and the associated alteration of the optical properties, the electronic properties are also changing with the formation of the $Ge_{1-x}Sn_x$, when compared to cubic germanium. Controlling the electronic properties is very important for the use of $Ge_{1-x}Sn_x$ as a channel material in transistors.[15] Alterations in the electronic properties are associated with changes of the valence band by either increasing the tin content or inducing strain. A significant change of the valance band structure is not expected upon increasing the tin content in the alloy due to the induction of a uniform volume strain.[17] However, uniaxial strain can change the valence band structure, as seen in figure 2, and therefore the electronic properties of the material.[17,35] Compared to room temperature photoreflectance (PR) spectra of unstrained $Ge_{1-x}Sn_x$ alloys (figure 4a-d) the room temperature spectra of compressively strained $Ge_{1-x}Sn_x$ alloys (figure 4e-g) show that

the degeneracy of the valence band is broken. The PR signals shown in figure 4e-g can be attributed to the transitions from light- and heavy-hole bands to the bottom of the Γ valley.
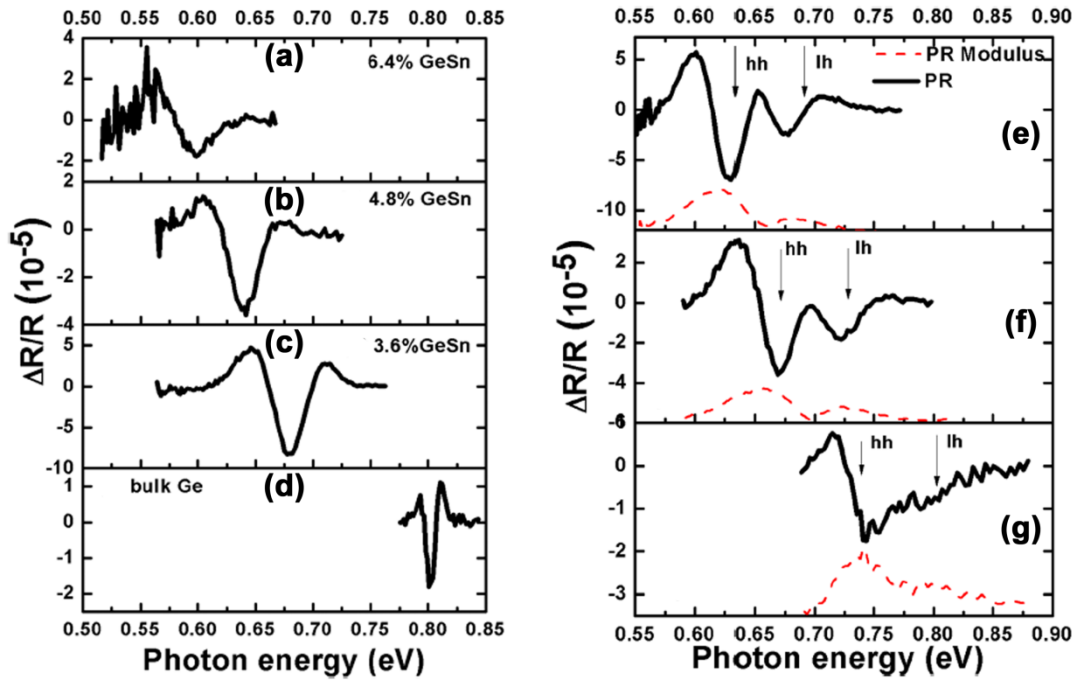
Figure 4: Room temperature PR spectra of unstrained $Ge_{1-x}Sn_x$ alloys for (a) x = 0.064, (b) x = 0.048, (c) x = 0.036 and (d) x = 0 and compressively strained $Ge_{1-x}Sn_x$ alloys for (e) x = 0.0632 (strain = -0.57 %), (f) x = 0.0528 (strain = -0.594 %) and (g) x = 0.0306 (strain = -0.513 %). The red dashed lines represent the calculated PR moduli.[36] Reproduced with permission from AIP Publishing LLC.[36]

As mentioned before, the most challenging aspect arising in the synthesis of the metastable direct band gap group 14 alloys is the kinetic control of the process. In thin film techniques the metastable product is only accessible under controlled process conditions, including temperature and precursor supply.[37] Chemical vapour deposition (CVD) and molecular beam epitaxy (MBE) are the techniques of choice to achieve a kinetically controlled synthesis.[20,35,38-40]
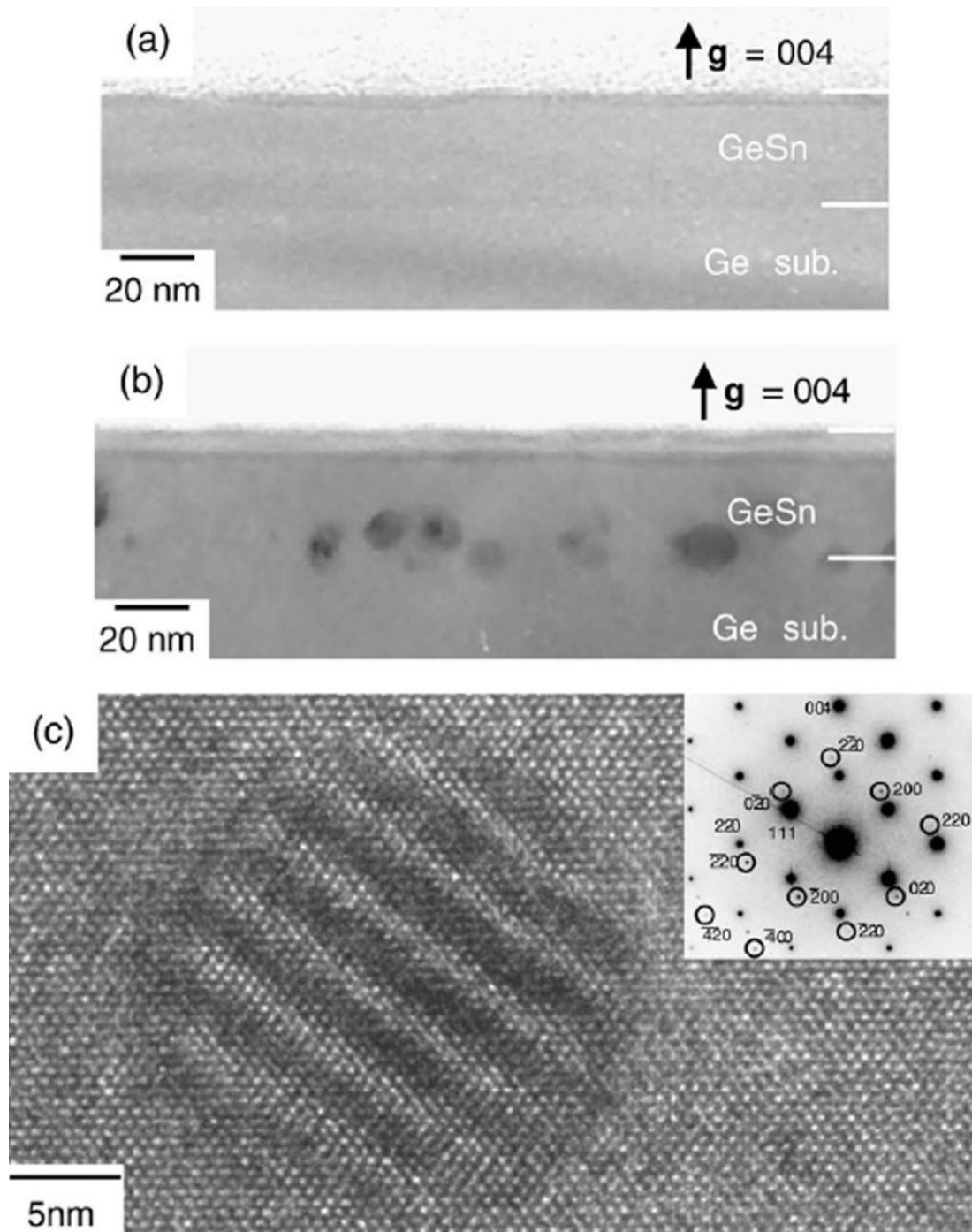
Figure 5: XTEM images of (a) as-grown and (b) post-deposition annealed $Ge_{0.92}Sn_{0.08}$ layers on Ge. (c) HRTEM image of the spherical dot shown in (b) with an obvious Moiré pattern. The inset shows corresponding selected area electron diffraction (SAED).[41] Reproduced with permission from Elsevier.[41]

Kinetically controlled syntheses are performed at low temperatures to decrease the diffusion rate. A high diffusion rate of the alloying atoms would lead to the thermodynamically stable product and thus segregation/phase separation would occur.[37] Segregation, which is essentially a spinoidal decomposition, can be observed when successfully grown $Ge_{1-x}Sn_x$ layers are heat treated at temperatures around 600 °C (figure 5).[41] Also Chen *et al.* observed changes in the properties of $Ge_{1-x}Sn_x$ layers after annealing treatments at 450-500 °C due to tin surface segregation.[42] A small diffusion length and a high growth rate lead to the incorporation of tin in the germanium matrix, which is similar to a statistical process, with control over the composition by the ratio of the supplied species.[23] Therefore, the ratio of the precursors, their decomposition rates, the process temperature and the growth rate are very important parameters for such a kinetically controlled process.[5]

2.2 Nanowire growth

For several fields of applications a large interaction zone/area with the environment is very important for a materials performance. A large interaction area is equivalent with a high surface-to-volume ratio. These facts make the synthesis of nanostructured materials, including nanowires, to a very interesting field of research. The challenge nowadays is to control and tailor the morphology as well as the composition of the desired materials. Besides these perceptions, it is well known that in the nano-sized regime, quantum confinement effects can be observed. These effects change the properties of the materials drastically.

A controlled synthesis of nanostructures in terms of the shape and composition is essential to improve materials properties. This work is focused on the synthesis of semiconductor nanowires and therefore the most common mechanisms to grow nanowires via bottom-up methods are discussed in this chapter. In general, the synthesis of nanowires can be achieved either by bottom-up or top-down approaches.

2.2.1 Top-down technique

The most common top-down method for producing one-dimensional materials is chemical etching using suitable masks. It is well known, that the different surfaces of a crystal have different surface energies. A high surface energy is equal to a high reactivity of the surface atoms due to their unsaturated coordination spheres. That is the reason, why etching is a very selective process and the etch rate is dependent on the crystal orientation. The knowledge about the surface reactivity of the desired material with certain etching agents enables the controlled removal of matter from a bulk material. Therefore, elongated structures can be formed on a surface by the combination of chemical etching and appropriate masking techniques.[43] The main disadvantage of top-down methods is the low throughput and the higher surface roughness when compared to bottom-up methods. However, the formation of top-down produced nanowires is very reproducible including (i) very minor variations in shape, (ii) controllable pre-determined crystal quality and doping level and (iii) an excellent control over their location. These advantages over the bottom-up method justify the time consuming fabrication process for certain applications; however, the bottom-up strategy can compete and even excel the top-down fabrication strategy for other applications. Examples include the localised heating of a substrate enabling the selective production of nanowires for sensor applications.[44]

2.2.2 Bottom-up technique

The bottom-up technique is based on the buildup of a material from small subunits. The subunits are usually provided *in situ* through the decomposition of a precursor, a chemical reaction or the evaporation of the desired element. The bottom-up method for the synthesis of nanowires can be divided into the non-metal and the metal seeded growth strategies.

2.2.2.1 Non-metal seeded growth

In the non-metal seeded growth no external metal seed is needed to induce the growth of nanowires. The subunits for the formation of the material are transported via the gas phase and can adsorb on the surface, where they are able to diffuse. Defects, including screw-dislocations, differences in the crystal surface energies and also self-seeding processes can induce the formation of a nucleus that evolves into a nanowire.[43]

An early example for nanowire growth from screw-dislocations is the formation of mercury whiskers.[45] The mechanism of the elongation of these whiskers can be described as a layer-by-layer growth along a srew-dislocation. This procedure can also be used to form ZnO nanowires on III/V semiconductor surfaces.[46]

2.2.2.2 Metal seeded growth

In a metal seeded growth of nanowires, the nanowires are usually nucleating from the metal particle. In addition, the metal seed can act as a reservoir for the subunits of the growing material and thus help to elongate the structure by a continuous supply of the units, while the nanowire material is growing at the metal-solid interface. The main advantage of the metal seeded growth is the good control of the nanowire diameter and the selectivity of the nucleation position. The most common growth mechanisms can be discussed in relation to the medium, gaseous or liquid, in which the process is performed and the state of the metal seed during growth.

2.2.2.2.1 Gas phase based process

Among all gas phase procedures for nanowire growth, CVD is the most powerful and popular technique for the controlled synthesis of semiconductor nanowires via a bottom-up method due to the excellent control over the process

parameters. Depending on the chosen precursor and temperature, nanowires with good quality in terms of purity, crystallinity and surface roughness can be produced.

In CVD processes two setups, the hot wall and the cold wall reactor type, should be considered when this growth technique is employed. The main difference between these two reactors is the heating up of the substrate and the potential decomposition on the sidewalls. In the cold wall reactor the substrate is heated up directly. Therefore, the wall of the reactor remains at lower temperatures, which minimises the nucleation events on the wall surface. In the hot wall reactor the substrate is heated up indirectly. Nucleation on the wall surface cannot be excluded/avoided in this setup.[47]

There are some requirements on the precursor for a successful CVD process. First of all the vapour pressure of the precursor has to be high enough to ensure a sufficiently high mass transport in the gas phase. In addition, the decomposition of the precursor should provide the subunits of the nanowire material and volatile byproducts to avoid contamination. Alternative reaction paths of the precursor are usually not beneficial for the process or much more difficult to control.

The deposition can be performed under different pressures spanning from ultra-high vacuum to atmospheric pressure. The pressure variation changes the mean free path of the molecules in the gas phase and also the thickness of the boundary layer on top of the substrate, through which the precursor and the decomposition products have to diffuse.[47] The mean free path is the average length a particle is able to translate in a phase, without colliding with another particle. These collisions can induce nucleation events, which are essential in the deposition of materials. By reducing the pressure, the possibility of nucleation in the gas phase is minimised compared to nucleation on the surface of the substrate due to the differences in the diffusion lengths. The diffusion length of adsorbed precursor molecules and decomposition products on the substrate or nanowire surface is a function of temperature. Increasing the temperature can therefore enforce the nucleation to occur preferentially on areas dictated by the metal seed and decrease secondary nucleation events due to the higher diffusion length at higher temperatures. There is another effect, which counteracts the influence of the temperature dependence of the diffusion length. The diffusion length is also a function of the particle concentration on the surface. The particle concentration on

the surface increases with raising temperature due to the quicker decomposition of the precursor. In addition, the substrate material is an important factor for the diffusion length, because different bond strength of adsorbates and the substrate material influence the diffusion. Taking all these influencing parameters into account, there is sometimes a rather small window for an optimal nanowire synthesis.[43,47]

In addition, a catalytic activity of the metal seed on the decomposition kinetics of the precursor has to be considered for the growth process. This property of the metal seed produces a concentration gradient, which is also beneficial for the selective nucleation and growth of the nanowires.[48] Two growth mechanisms have to be considered for metal seeded nanowire growth in a CVD process, which essentially differ in the aggregate state of the metal during growth.

2.2.2.2.1.1 Vapour-Liquid-Solid (VLS) mechanism

The VLS mechanism is the most well-known nanowire growth process and was first described by Wagner and Ellis in 1964 for gold-supported silicon nanowire growth.[49] The metal seed is initially forming a liquid alloy of eutectic composition with the decomposition product of the precursor. The material starts to nucleate at the liquid-solid interface between the alloy particle and the substrate as soon as the alloy particle is supersaturated. Once a nucleus exists, the crystal growth proceeds as long as sufficient vapour pressure of the precursor is available.

Advantages of using metal seeds for growing nanowires include the possibility of controlling the diameter, limited surface roughness and the pre-definition of the nanowire position. A disadvantage of the VLS growth is the possible incorporation of the metal from the growth promoter in the crystal lattice of the desired material due to the fast growth rate.[50-51] The incorporation of these atoms can lead to undesired changes of the material properties.

2.2.2.2.1.2 Vapour-Solid-Solid (VSS) mechanism

The term vapour-solid-solid growth is used, when the seed metal is not building a liquid alloy with the decomposition product of the precursor at the desired process temperature, but a solid alloy or compound instead. The principle is comparable to the VLS growth, but the seed remains in the solid state during the whole synthesis. The elongation is promoted by material transport to the solid-solid interface growth front by diffusion of the subunits (i) on the surface of the solid seed, (ii) on the surface of the nanowire body and (iii) through the solid seed only when a solid solution of the nanowire material and the growth seed can be expected.
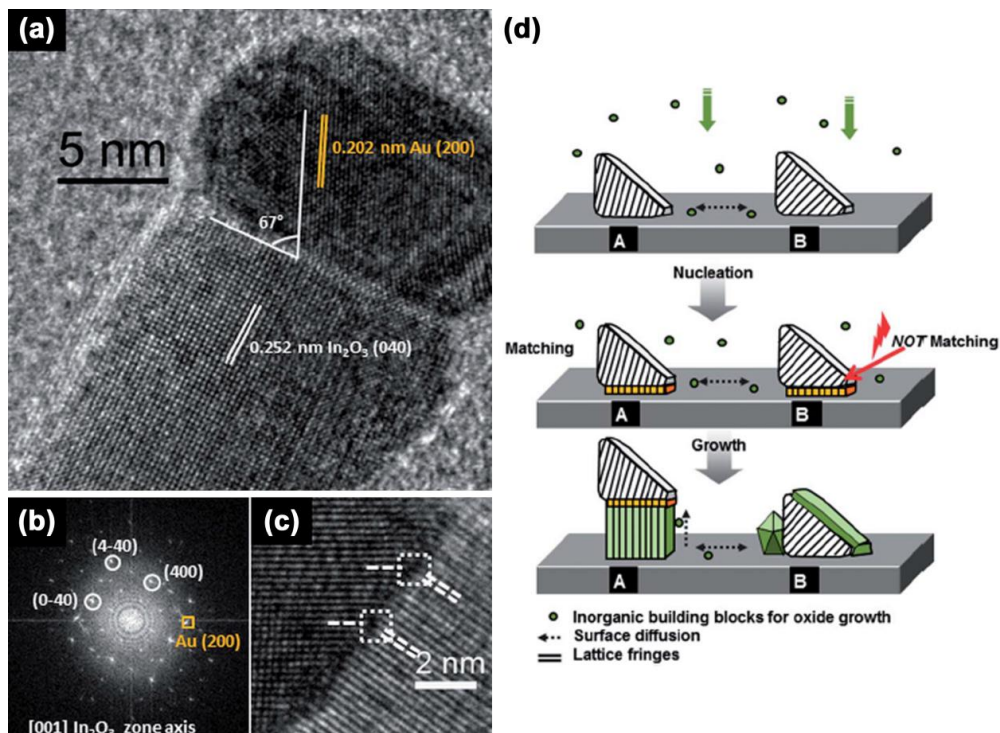
Figure 6: (a) HRTEM image of an In_2O_3 nanowire and the respective gold growth seed. (b) The fast Fourier transform (FFT) pattern shows the power spectrum of the wire in (a) with assigned reflections and the lattice matching of the gold seed and the In_2O_3 nanowire. (c) In the HRTEM image the occurrence of one-dimensional defects at the Au-In_2O_3 interface are highlighted. (d) Schematic illustration of (A) the crystal guided VSS growth and (B) the absence of 1D nanostructure formation, when the lattice parameters in the orientation of the Au crystal do not match with the In_2O_3 lattice.[52]

Nanowires produced by the vapour-solid-solid growth are known to be less contaminated with the metal from the seed.[53] However, the influence of the seed orientation in the solid state is often neglected. We were able to demonstrate that the epitaxial relationship between solid Au particles and growing In_2O_3 nanowires is very important for a VSS growth procedure at low temperatures (figure 6).[52] Only a specific fraction of all seeds in a vapour-solid-solid system is active, but the number can be increased by pre-orientation on a growth substrate. This pre-orientation increases the yield of nanowires due to more active nucleation centres.

2.2.2.2.2 Solution based process

The main difference of a solution based bottom-up method to gas phase processes is the decreased diffusion length of the precursor and its decomposition products. Generally this leads to an increase of secondary nucleation events, which makes solution based processes more difficult to control. The classical nucleation theory shows that the production of monodisperse particles needs a highly controlled system. For the nanowire growth this theory implies that a wide range of products is usually obtained in such processes due to the lack of control in most cases. Therefore, the nucleation step and post-growth separation are important topics in the solution based nanowire synthesis.

The main advantage of solution based processes is the broader range of suitable precursors. The only requirements on the precursor are a good solubility in the chosen solvent, a clean decomposition path and a decomposition temperature below the boiling point of the solvent. Usually the solvent has a high boiling point and is stable at higher temperatures, unless high pressure vessels allowing supercritical synthesis conditions.[54-55] In solution based synthesis the metal seed is usually stabilised using surfactants to avoid coalescence and induce solubility. For an industrial mass production of nanowires a solution based process is of course a good choice due to the simple handling of solutions and easier upscaling potential.

Similar to the gas phase process, the solution based process can be better described when different growth scenarios are described separately.

2.2.2.2.2.1 Solution-Liquid-Solid (SLS) mechanism

Similar to the VLS growth in the gas phase process, the SLS growth can be described by exchanging the gas phase with the liquid phase and therefore a reduction of the diffusion length and the absence of a substrate acting as nucleation side. In the SLS growth strategy a particle of a low melting metal (Au, Bi, In, Sn) is usually used as seed,[56-57] which can be produced *in situ* or *ex situ*. *In situ* processes can contain one step or multi step syntheses. A one step synthesis is very difficult to realise due to some requirements including the differences in decomposition temperatures for the seed and nanowire materials, respectively. Although it is not trivial to implement a one step *in situ* process, it is worth striving for due to the simplicity, once all the requirements are fulfilled and the process is adjusted.[58] A two-step process often includes an injection in a high boiling point solvent at elevated temperatures leading to a temperature gradient during the nanowire nucleation and growth.[59-60] More sophisticated microfluidic cells can help to avoid the aforementioned shortcomings and can even enable the synthesis of segmented nanowires by the SLS mechanism at the cost of a complex process setup.[61]

A special case of the SLS growth is the supercritical fluid-liquid-solid growth (SFLS). At high pressure (up to 300 bar) the used solvents can become supercritical fluids at temperatures above the critical temperature. The main difference to the SLS growth is again the change in the diffusion length. Above the critical point the liquid phase and the gas phase cannot be distinguished, therefore it is obvious, that the diffusion length in the supercritical fluid has to be somewhere between the diffusion length in the liquid and the gas phase.[55,62-63]

2.2.2.2.2.2 Solution-Solid-Solid (SSS) mechanism

The SSS growth mechanism is very similar to the VSS growth. As mentioned before, the only difference is the exchange of the gas phase with the liquid phase. All the relevant points discussed in chapter 2.2.2.2.1.2 and 2.2.2.2.2.1 are valid for the SSS growth as well. A common metal seed for this kind of growth is Ni. Germanium

nanowires have been grown successfully in a supercritical fluid by a supercritical fluid-solid-solid growth mechanism (SFSS), which also allowed a size selective synthesis of nanowires in high density.[53,64]

2.3 Microwave synthesis

Economically and environmentally friendly working is a big topic nowadays. Microwave-assisted methods have high potential to improve the efficiency of synthesis procedures. Although there are still some problems that have to be solved, microwave-assisted synthesis can be used in laboratory as well as on the industrial scale.

However, a lot of research efforts should be devoted to the fundamental processes occurring during the irradiation with microwaves. A literature survey shows, that there are still a few uncertainties on the effects caused by microwave irradiation.[65] The status quo of the use of microwaves for inorganic material synthesis is discussed in this chapter.

Microwaves are electromagnetic waves with frequencies in the range of 300 MHz to 300 GHz.[65] These energies are not high enough to excite electrons or even cleave bonds, but the electric field induced by the electromagnetic wave leads to a polarisation of the irradiated molecules. The polarisation is caused by the rotation of dipoles. This leads to a heating of the irradiated molecules due to the friction between neighbouring quickly rotating molecules and the increase in the translational energy of molecules next to rotating molecules.[66] Compared to conventional heating, the molecules are heated up directly with microwave irradiation. The conventional way of heating up consists of the heat transfer from a heat source to the reactor and its content via thermal conduction. Figure 7 shows the temperature profile of a reactor and its content either using microwaves or an oil bath for heating up.[67]
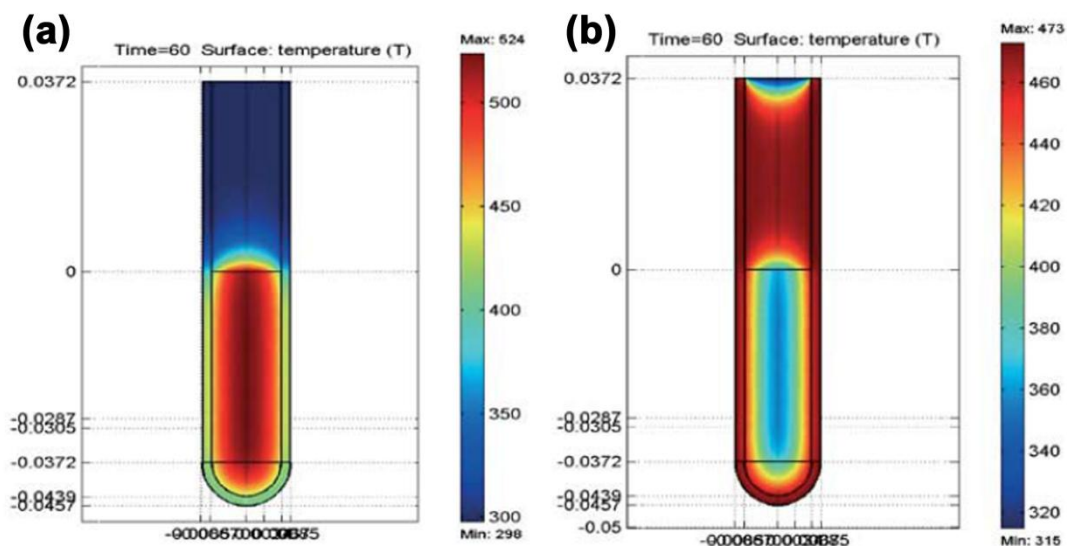
Figure 7: Temperature profile of a vessel heated by (a) microwave irradiation and (b) conventional heating in an oil-bath. In (a) the reaction volume is heated simultaneously, while in (b) the wall of the vessel is heated first and a temperature gradient in the reaction volume occurs.[67] Reproduced with permission from Springer.[67]

However, other important observations related to the microwave-assisted synthesis procedures include reports on an acceleration of reactions/processes[68-70] and increased yields.[71] Compared to conventional heating, the temperature increase using microwaves is very quick and reaction times are very short, which leads to a reduction of energy consumption.[65] In addition, the crystal growth rate and the nucleation rate are different for microwave and conventional heating.[68] The different temperature profiles of the samples mentioned above already suggest a variation of the processes and experimental results support the theoretical assumptions.
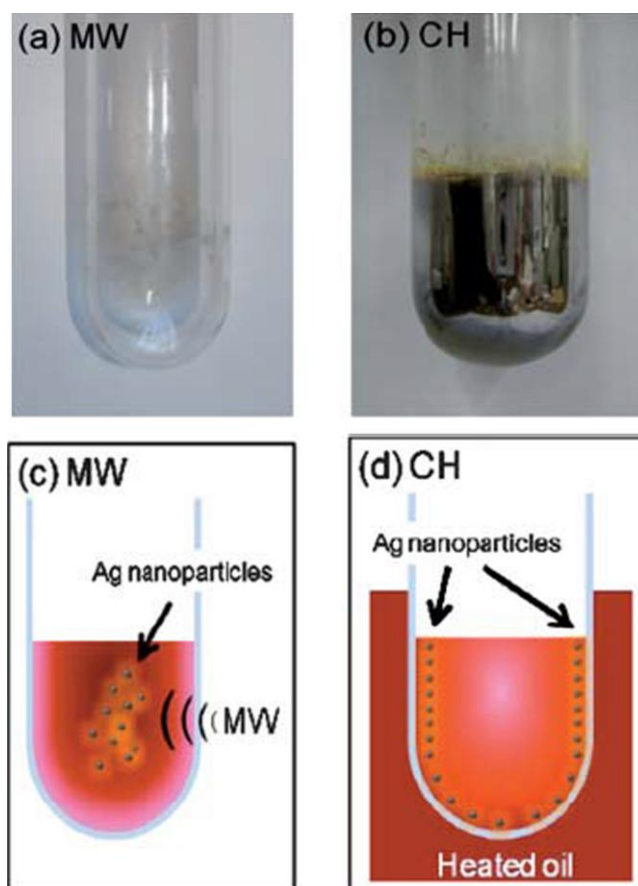
Figure 8: Reaction vessel after (a) microwave irradiation for 4 min and (b) conventional heating in an oil-bath for 5 min. The reactions were carried out without stirring the diamminesilver(I) ion containing aqueous solution, 60 mM, with 0.05 % w/v carboxymethylcellulose. Schematic illustration of the different temperature profiles and nucleation processes when undertaking the reaction under (c) microwave irradiation or (d) conventional heating.[72] Reproduced with permission from the Royal Society of Chemistry.[72]

For instance, during the synthesis of Ag particles by heating up an aqueous solution of carboxymethylcellulose and diamminesilver(I) ions with microwaves, no decomposition on the reactor wall is observed. The absence of a silver film is a direct result of the lower temperature of the wall compared to the reactor content preventing the nucleation on the solid-liquid interface in this thermally activated process (figure 8).[72] Obviously, the diameter of the reactor plays a significant role in the penetration depth of the microwaves in the liquid and the resulting inhomogeneity would influence the targeted process. However, controlled stirring of the reactor

content can lead to an entirely homogeneous temperature profile inside the reactor, which is impossible to reach using a conventional heating system, where the heat has to be transferred through the interfaces.

The explanations of the effects caused by microwaves can be divided into two categories including (i) the specific and (ii) the non-thermal microwave effect. Specific microwave effects are thermal effects, but are not observed in conventional heated systems. It includes the presence of so called "hot spots", which are selectively heated areas due to the different polarity of the present chemicals. Non-thermal microwave effects are caused by the direct interaction of microwaves with distinct substances inside the sample. It is important to notice, that these effects cannot be attributed to thermal effects.[73]

Although some of these effects have been discussed in literature, there are some hints that the observed results can all be related to thermal/kinetic effects due to the high reaction temperatures, which can be attained rapidly.[74-77] The misinterpretations are caused by the difficulty of comparing conventional to microwave-assisted heating. The fundamental mechanisms of microwave-assisted heating can only be deciphered using a setup providing similar process conditions for both heating methods.[65] Obermayer *et al.* showed a possibility to enable the comparison of the conventional and the microwave-assisted heating.[75] In this study a silicon carbide reaction vessel was used, which was initially suggested by Kremsner *et al.* due to the strong microwave absorption, the chemical inertness, the high melting point and the low thermal expansion coefficient.[78] The microwaves are converted to thermal energy by the strong absorbing silicon carbide, which is then transferred to the reaction mixture via conduction phenomena. Furthermore, the microwaves are not able to directly interact with the content of the reaction vessel with this setup.[78] This enables a meaningful comparison of microwave and conventional heating.

All in all microwave-assisted heating is a promising method to do economically and environmentally friendly synthesis and the potential in chemical and materials synthesis is obvious.

2.4 Devices

This chapter will focus on the use of germanium and its alloys for electronic and optical devices.[14-15,43,79-82] Relaxed germanium has a higher hole mobility compared to relaxed silicon and other materials and is therefore an interesting candidate for the implementation in electronic devices.[17] Introducing biaxial compressive strain on $Ge_{1-x}Sn_x$ by growing a thin layer on a germanium virtual substrate is a possibility to enhance the electronic properties due to an increase of the mobility of electrons and holes. These improvements are necessary to reach higher performances and lower power consumptions in microelectronics. As a representative for electronic devices the p-channel metal-oxide-semiconductor field-effect transistor (PMOSFET) will be discussed in this chapter. Due to the band gap of 0.66 eV, also the optical properties of germanium would be interesting if it was a direct band gap material.[7] Germanium is an indirect band gap material and is therefore not efficient enough to be applicable in optical devices. Alloying germanium with more than 6.5-11 % of tin, leads to the transition in a direct band gap material.[1-2,14] For instance, lasers based on $Ge_{1-x}Sn_x$ emit in the mid-IR range, which is a desirable goal due to the targeted applications in medical diagnostics and high-speed communications.[29,83]

2.4.1 Metal-oxide-semiconductor field-effect transistor (MOSFET)

A MOSFET is an electronic device, which facilitates to switch whether an electric current is able to flow from drain to source or not, by applying a voltage between the gate and the bulk. Nowadays, the term metal-oxide-semiconductor is not always correct, but still very common, although the gate material does not have to be a metal and the gate dielectric does not have to be an oxide. The term insulated-gate field-effect transistor (IGFET) can be used to keep the description more universal. The currently produced most simple MOSFETs in industry consist of silicon (bulk), silicon dioxide (gate dielectric) and polycrystalline silicon (gate). Depending on the type of doping of the channel material, two kinds of devices, namely p- or n-channel MOSFETs, can be differentiated.

The general principle of a MOSFET relies on p-n-p or n-p-n junctions. The resistance of such a configuration is very high due to the depletion zone at the p-n junctions and an effective charge transfer between the source and the drain of the device is not possible. The gate and the bulk are separated by a dielectric and this part of the device behaves like a capacitor. Applying a voltage between the gate and the bulk leads to an accumulation of the minority charge carriers at the interface. The minority charge carriers recombine with the majority charge carriers and an inversion layer forms at voltages higher than the threshold voltage. The semiconductor behaviour is inverted in a narrow region at the bulk-dielectric interface and the former minority charge carriers are in the majority in proximity to this interface. This scenario enables an electric current to flow from source to drain.
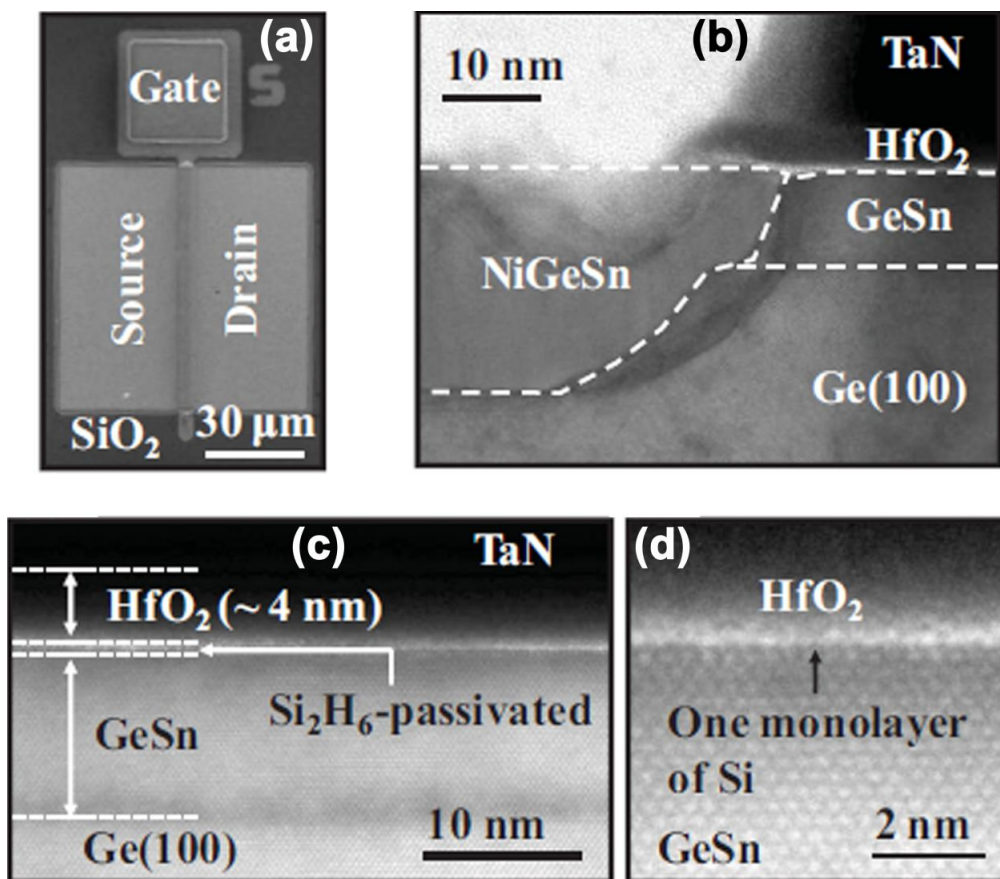

Figure 9: (a) shows a top view scanning electron microscopy (SEM) image of a MOSFET with a gate length of 5 µm. (b) Source/drain region with NiGeSn as the contact, $Ge_{1-x}Sn_x$ as the channel and a TaN gate. (c) HRTEM image of the channel region. (d) HRTEM image illustrates the high quality of the $Ge_{1-x}Sn_x$/Si/HfO$_2$ interface.[15] Reproduced with permission from IEEE.[15]

The main advantage of a $Ge_{1-x}Sn_x$ MOSFET is the increased hole mobility compared to other materials leading to a high drain current. In figure 9 the first high mobility $Ge_{1-x}Sn_x$ p-type MOSFET is shown. It is reported, that the hole mobility is 66 % higher and the source/drain resistance 64 % lower than a Ge control device.[15] The improvement of transistors for microelectronics is a necessary process according to Moore's law requiring intense research on this topic.

2.4.2 Laser

The implementation of optical devices on chips is a very active field of research but remains a challenge. The silicon on insulator (SOI) technology enables to guide a wave on a chip by internal reflection due to the transparency of silicon for infrared light. These waveguides create the conditions which are necessary to produce lasers and high-speed communications on a chip.[4] For this purpose the near- and mid-IR radiation is an interesting wavelength for the implementation of these goals. As already mentioned before, $Ge_{1-x}Sn_x$ with high tin content is a suitable material in terms of the band gap and the compatibility with silicon processing. In this respect, a good crystal quality of the active material is necessary to obtain high emission efficiency. Defects are able to decrease the emission efficiency and thus their number should be as small as possible, which is challenging for growing $Ge_{1-x}Sn_x$ layers on silicon or germanium buffers due to the large lattice mismatch.[4-5,84-85]

The first proof of concept for $Ge_{1-x}Sn_x$ based lasers in literature shows that a good quality of the $Ge_{1-x}Sn_x$ layer is the basic requirement to observe theoretically predicted results.[14,33] Although dislocations appear by growing a $Ge_{1-x}Sn_x$ layer on a virtual germanium substrate, they do not decline the material quality, due to their spatial restriction to the interface and absence in the bulk $Ge_{1-x}Sn_x$ layer.
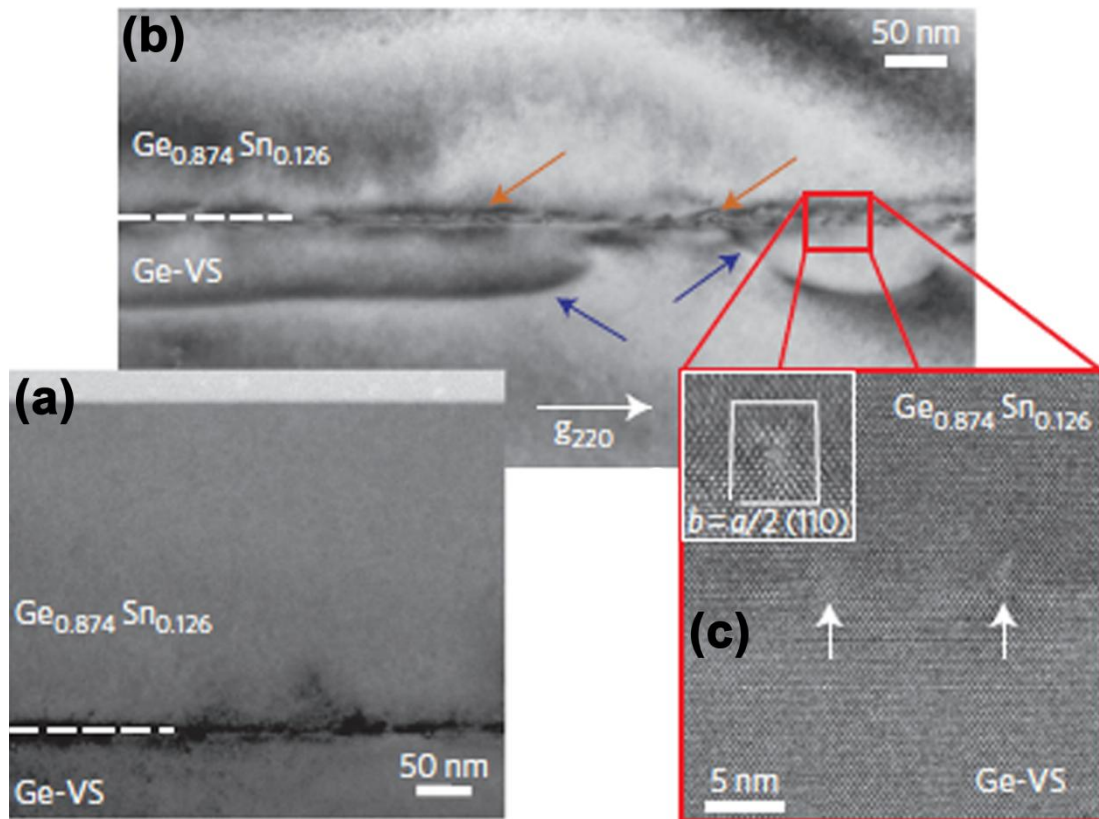
Figure 10: (a) shows a XTEM image of a $Ge_{0.874}Sn_{0.126}$ layer. In (b) dislocation loops (blue arrows) are just visible below the $Ge_{0.874}Sn_{0.126}$/Ge interface (orange arrows) in the Ge buffer. (c) The HRTEM image of the interface.[14] Reproduced with permission from Nature Publishing Group.[14]

There are still some fundamental problems and a lot of research must be done in future to reach the goal of the implementation of a mid-IR laser on a chip. The primary step therefore is to further advance the growth of a good quality $Ge_{1-x}Sn_x$ material on silicon or other substrates and also gain knowledge of the general formation mechanism of $Ge_{1-x}Sn_x$ nanostructures.

3 Motivation and targeted outcome

The specific properties of $Ge_{1-x}Sn_x$ have been discussed in the introduction. However, apart from the thin film growth strategies, only very limited data are published for the growth of nanostructured $Ge_{1-x}Sn_x$ alloys. There was literately no report on the bottom-up growth of one-dimensional nanostructured $Ge_{1-x}Sn_x$ with high tin content. The main goal of this thesis was the growth of metastable $Ge_{1-x}Sn_x$ nanowires with high tin content in absence of the common noble metal growth promoters and structure guiding substrate materials. According to the binary phase diagram of Ge/Sn the maximum of the solid solubility of tin in germanium is thermodynamically limited to a mole fraction of about 0.011.[16] Therefore, a thermodynamically controlled process was not targeted in this case and the process should proceed at low temperatures under kinetic control.

4 Results and discussion

A literature survey shows that for solution based synthesis temperatures above 250 °C are usually required to grow crystalline germanium nanocrystals via thermal decomposition of organogermanes by conventional heating or reduction of germanium iodides.[86-90] In addition, strong reducing agents enable the formation of germanium nanocrystals by the reduction of germanium halides at much lower temperatures.[91-93] The disadvantage of strong reducing agents for the synthesis of elongated germanium nanocrystals is the lack of process control for the elongation of a crystal and the difficulties concerning the separation and purification process. The use of reducing agents with germanium iodides in the presence of amines is not as simple as often explained in literature. A close inspection of the synthesis parameters suggests that often the germanium iodide is not reduced directly by the reducing agent but a reaction with the primary amine is induced. Even the heating up of germanium iodides and primary amines without using reducing agents could lead to the formation of imides and/or amides.[94] This could explain the often mentioned change in the colour of the solution.[95-96] The importance of the amine for the synthesis of germanium nanocrystals was already recognised by Muthuswamy *et al.*, but no identification of the intermediates has been described in literature.[95]

For the growth of germanium nanostructures in the temperature range from 250 to 300 °C higher tin contents in the germanium lattice are observed in the presence of tin precursors due to a kinetically controlled growth regime.[97-98] The supply and decomposition rate of the precursor species are very important factors in a kinetically controlled process and will be discussed in the next chapter.

Homogeneous nucleation is substantial for the controlled growth of low dimensional structures. A liquid injection process has the disadvantage of creating a temperature gradient, when injecting the precursor solution into the solvent but also allows the formation of a larger number of nuclei, which is beneficial if the synthesis of nanoparticles with small size-distribution is targeted. However, nucleation at the wall of the reaction vessel can lead to a broad range of products.

The problems including the necessity of high temperatures and the lack of control concerning the nucleation process can be eliminated by using microwave

radiation for the selective heating of the reaction volume. Side wall nucleation effects and temperature gradients caused by the injection can be excluded in this case. Muthuswamy *et al.* compared the difference of conventional and microwave heating for the synthesis of germanium nanocrystals. Microwave irradiation of an oleylamine/germanium iodide mixture leads to germanium nanocrystals, while conventional heating leads to amorphous germanium at temperatures near 210 °C. The authors of this study suggest that the selective heating of the precursor molecules by microwaves leads to these observations.[95]

4.1 Precursor

The understanding of the precursor species plays a very important role in materials synthesis and especially in the here presented work. Many studies focusing on the solution based synthesis of germanium nanostructures are based on germanium halides in combination with a primary amine. The role of the primary amine is attributed to act as a binding ligand and reducing agent.[95,99] However, the exact process including the primary amine is not clearly identified to date.

The chemical system chosen for the aim of synthesising $Ge_{1-x}Sn_x$ nanowires consists of bis[bis(trimethylsilyl)amino]germanium(II) ($Ge(HMDS)_2$), bis[bis(trimethylsilyl)amino]tin(II) ($Sn(HMDS)_2$) and dodecylamine. Based on studies concerning the formation of oligomeric group 14 imides the role of the primary amine in the precursor mixture used for this thesis was identified.[100-103] A ligand exchange reaction between the metal amide and dodecylamine can lead to the formation of group 14 imido cubanes. Sterically demanding primary amines, such as tert-butylamine, result in the formation of seco-norcubanes, which can be transferred to imido cubanes by either increasing the reaction time or raising the temperature. Moreover, the atomic radius and the electronegativity of the group 14 elements influence the reaction. The transformation to the thermodynamic most stable compound, the imido cubane, proceeds quicker with increasing atomic number of the group 14 elements.[101]

In this study, particular attention is paid to the specific reactions of the starting compounds before thermolysis and emerging intermediates. The desired SLS process for the formation of $Ge_{1-x}Sn_x$ nanowires requires a temperature near the eutectic temperature of about 230 °C.[16] Dodecylamine is used as a primary amine to ensure the formation of imido cubanes but also to act as a solvent due to its high boiling point. The alkyl chain of dodecylamine is not branched but quite long, which can be categorised in terms of sterical demand between tert-butylamine and methylamine. It has to be considered that both germanium and tin amide are present in the precursor mixture, which can lead to heterometallic imido cubanes similar to a study by Veith *et al.* about heterometallic group 14 imido cubanes.[101] In the case of the Ge/Sn system theoretically five different imido cubanes shown in figure 10 can be obtained.
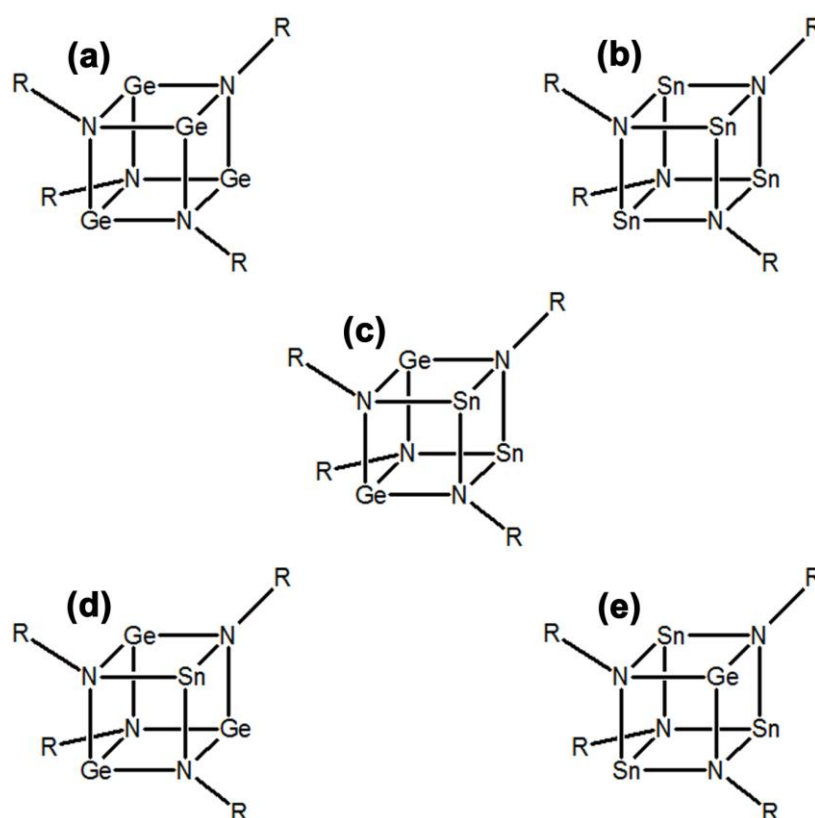
Figure 10: Theoretically possible cubanes formed by the reaction between $Sn(HMDS)_2$, $Ge(HMDS)_2$ and dodecylamine. The homometallic (a) Ge and (b) Sn imido cubanes and the heterometallic imido cubanes with Ge/Sn ratio of (c) 2:2, (d) 3:1 and (e) 1:3 are illustrated. The residue $R = C_{12}H_{25}$ in the case of using dodecylamine as the primary amine.

The formation of the heterometallic imido cubanes upon mixing of Sn(HMDS)$_2$, Ge(HMDS)$_2$ and dodecylamine in a 1:4:5 ratio is illustrated in figure 11. The ^{1}H-NMRs in figure 11 acquired after removal of the volatile components confirm the formation of the heterometallic imido cubanes. The different shifts of the α-CH signal can be assigned to changes in the chemical environment and electron density, which of course depend on the Ge/Sn ratio of the imido cubane. Assigning the shift of the α-CH signal to a specific imido cubane species is not trivial due to the inaccessibility of specific derivatives by the simple predetermination of the metal amide ratio. Veith *et al.* reported the same problem for the Sn/Pb system, which is explained by the weak Pb-N bond enabling rearrangement reactions. A solution would be the stepwise synthesis of the tin rich heterometallic imido cubane starting from a homometallic tin seco-norcubane. The synthesis of this amido/imido tin derivative requires the use of sterical demanding amines and provides the opportunity to close the cubane cage by adding a germanium precursor.[101] Obviously, rearrangement/scrambling reactions are enabled in the presence of dodecylamine and HMDS. Nevertheless, the mixture of imido cubane species seems to be essential for a successful Ge$_{1-x}$Sn$_x$ nanowire synthesis. The assignment of the α-CH signal to a certain imido cubane species is made possible by synthesising the homometallic imido cubanes shown in figure 11. However, only two signals can be assigned to the heterometallic imido cubane species. It is very likely that the heterometallic imido cubane with the Ge/Sn ratio of 2:2 is not present in the mixture due to the evaluation of the integrated signals. The α-CH signal of the germanium rich heterometallic imido cubane is shifted downfield while the α-CH signal of the tin rich heterometallic imido cubane is shifted upfield, when compared to the respective homometallic imido cubanes.
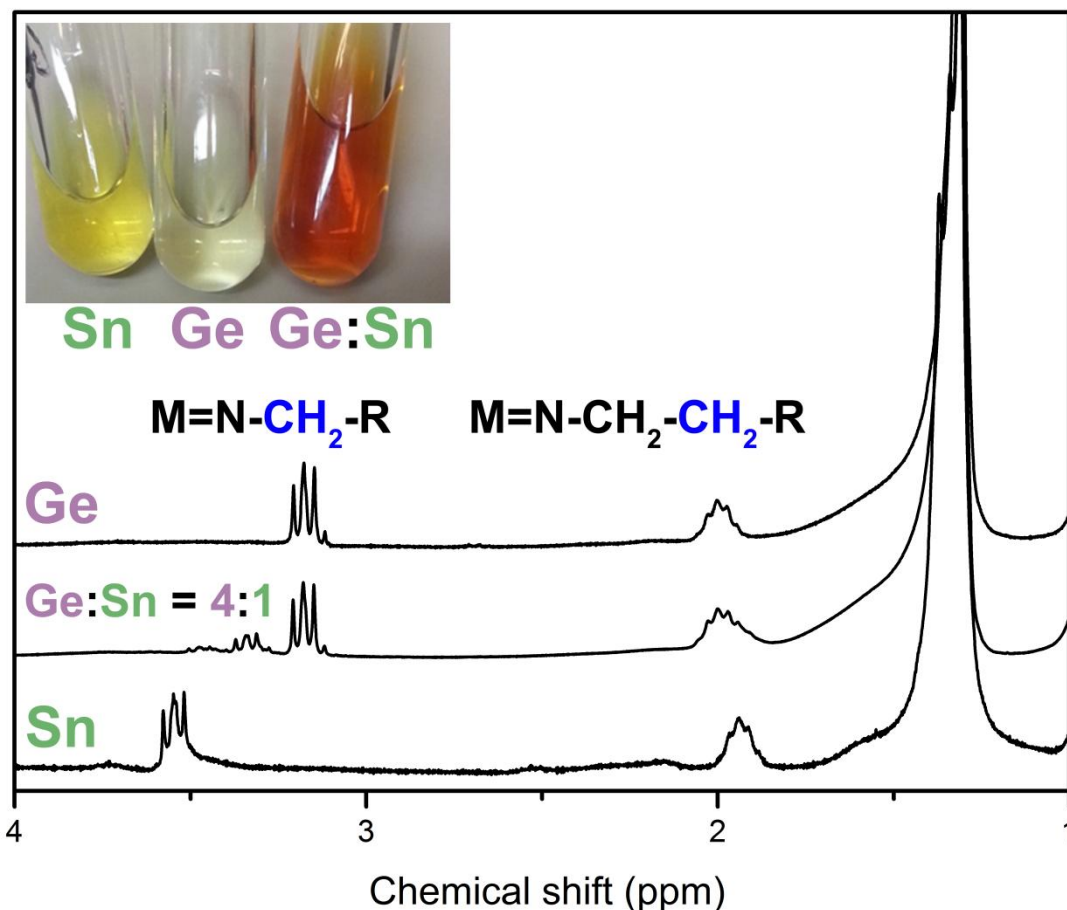
Figure 11: The photograph shows the colour of the homo- and heterometallic imido cubanes dissolved in dodecylamine. The ^{1}H-NMR spectra of the homometallic imido cubanes and the spectrum using a mixture of the metal amides as educts are presented.

However, it is very important to note that the condition of the chemical system during the heating step can differ due to the excess of dodecylamine and the presence of HMDS in the precursor mixture. The excess of amines can induce additional rearrangement reactions, which could lead to a change of the imido cubane derivative ratio in the material synthesis. The analysis of the process during the heating step is not trivial due to the dodecylamine, which is used in excess as a solvent.

The main advantage of using heterometallic imido cubanes for the synthesis of $Ge_{1-x}Sn_x$ structures via the thermal decomposition of the precursor is the spatial proximity of the germanium and tin species in the desired ratio. This makes the

formation of $Ge_{1-x}Sn_x$ structures/nuclei very likely in a kinetically controlled process. When two different sources for germanium and tin are supplied, the ratio of the germanium and tin species is a function of concentration and temperature, while the decomposition of single source precursors keeps the ratio of the supplied species fixed and allows a better control over the growth in a simple setup.

Very recently, Esteves *et al.* described the formation of $Ge_{1-x}Sn_x$ nanoparticles by reaction of germanium(II) iodide, tin(II) chloride and oleylamine at low temperatures and the injection of butyl lithium at 230 °C, which is followed by a heating up to 300 °C.[97] The concentration and metal ratio are comparable to those reported in this thesis, while a temperature gradient instead of a reaction at constant temperature was applied. In addition, the presence of hydrogen halides, which occur when group 14 halides react with primary amines, could lead to other products than imido cubanes similar to results by Veith *et al.* where the reaction of hydrogen chloride with tin imido cubane was studied.[94] These differences could account for the relatively low tin content of the $Ge_{1-x}Sn_x$ structures compared to the here presented study and point towards the importance of the heterometallic imido cubane species for the synthesis of $Ge_{1-x}Sn_x$ structures with high tin content.


4.2 Materials synthesis and characterisation

According to the binary phase diagram of Ge/Sn a temperature of 230 °C, which is near the eutectic temperature of the system was chosen for the synthesis of $Ge_{1-x}Sn_x$ nanowires.[16] In chapter 4.1 the role of dodecylamine as a ligand was already discussed. Moreover, the physical properties of dodecylamine are important parameters for the synthesis procedures. The vapour pressure of dodecylamine is very low in the desired temperature range for the synthesis, which is essential for the used setup to avoid large internal pressures in the reaction vessel. The contribution of the precursor to the heating process cannot be excluded due to the poorly microwave absorbing nature of dodecylamine. The absorption of microwaves by the precursor can lead to slight weakening of the bonds benefiting the desired decomposition of the precursor.

In the glove box $Ge(HMDS)_2$, $Sn(HMDS)_2$ and dodecylamine are mixed, which instantly leads to the formation of imido cubanes associated with a change of the colour (figure 11). Obviously, the ratio of the employed amides, the length of stirring, the temperature, the order of the added chemicals and of course the length of the decomposition influence the composition in the precursor mixture and have to be considered for a successful synthesis. The produced precursor mixture is placed in the microwave reactor and heated to 230 °C for 1-30 min. The combination of precursor and microwave irradiation enables the formation of $Ge_{1-x}Sn_x$ nanowires at comparable mild temperatures. After the decomposition a low yield of a dark grey solid can be separated from the mixture by centrifugation and washing with toluene. Dodecylamine binds strongly to the surface of germanium nanowires and should be removed in a subsequent process, when optical applications are targeted. Very likely, the presence of the amine plays a central role in the emission of $Ge_{1-x}Sn_x$ alloys due to the quenching of the core state emission by a charge transfer state as described for silicon nanocrystals.[104-105] Depending on the addressed criteria, which have to be considered for the production of the precursor mixture, different products can be obtained.

4.2.1 Material synthesis without pretreatment of the precursor mixture

First the products, which result from the decomposition of a precursor mixture without a pretreatment step are discussed. In chapter 6.2 detailed informations about the preparation of the precursor mixture are provided. Essential differences are the length of stirring and a temperature treatment step. Transmission electron microscopy (TEM) images of the different products obtained without pretreatment of the precursor mixture are summarised in figure 12. Interestingly, the obtained product morphology differs with the duration of the decomposition at high temperatures. Figure 12a shows nanowires with an increasing diameter, while in figure 12b a segment with constant diameter follows the initial part. In figure 12c an additional segment with diminishing diameter can be observed.
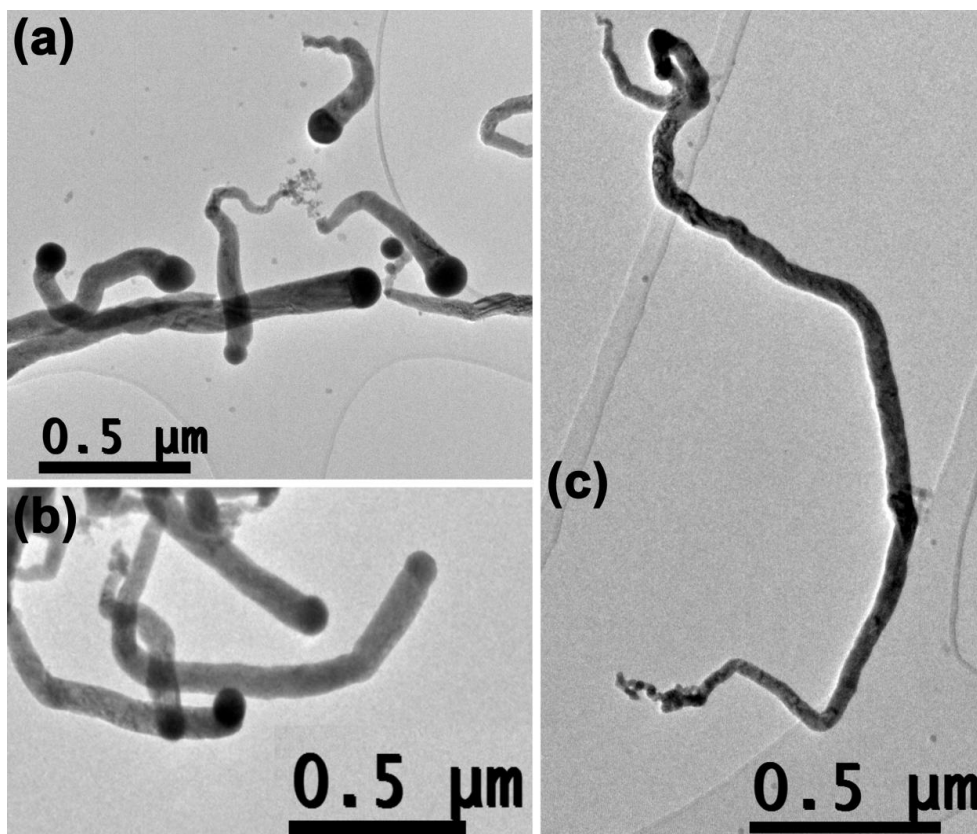
Figure 12: TEM images of the different products obtained by the decomposition of the precursor mixture without pretreatment. (a) shows nanowires with an expanding diameter. A constant diameter segment following the initial part of the nanowire is shown in (b). In (c) an additional segment with diminishing diameter extends the constant diameter segment of the nanowire and terminates the growth.

The different morphologies of the products can be attributed to the length of the decomposition step. A short duration of the decomposition step leads to the products shown in figure 12a + b. If the length of the decomposition step is increased nanowires like the ones in figure 12c can be obtained. These results suggest a strong impact of the availability of the different precursor species during the growth on the morphology of the nanowires.

The products, which result from a precursor mixture without pretreatment, are not suitable for the desired applications due to a change in the diameter along the nanowire axis, a rough surface or an accumulation of defects. However, the energy dispersive X-ray spectroscopy (EDX) elemental mapping images in figure 13 confirm the desired growth via the SLS mechanism. The semicircular tin rich nucleus at the

growth front serves as a first indication of a nucleation site. In addition, the mapping reveals a well dispersed tin content in the germanium nanowire body without accumulation in specific parts, which would be a sign of phase separation.
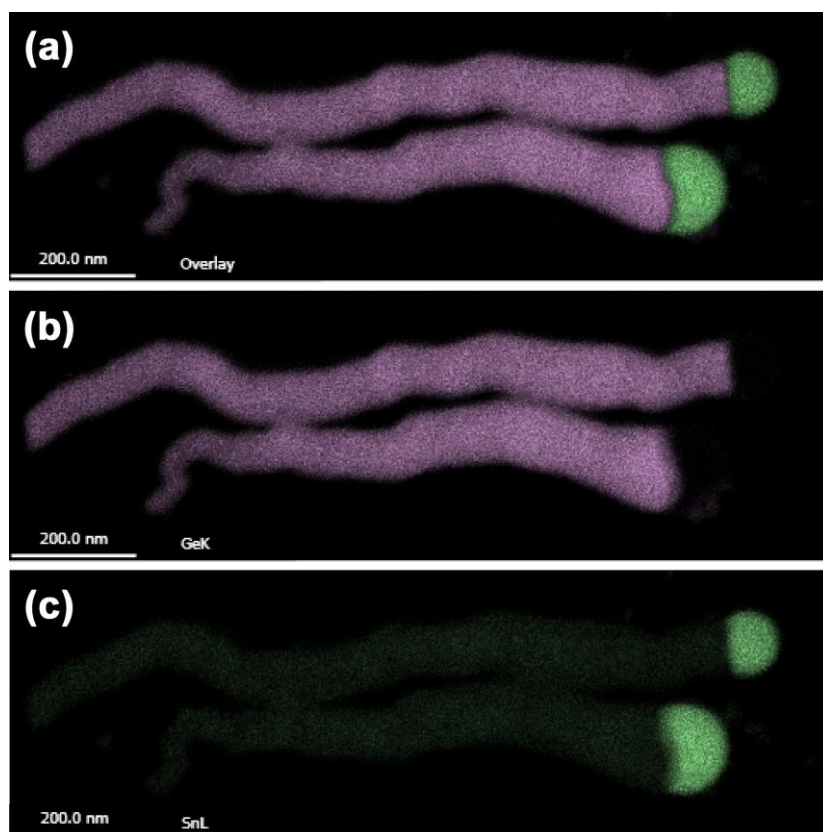
Figure 13: EDX elemental mapping of $Ge_{1-x}Sn_x$ nanowires without a pretreatment of the precursor mixture and a short decomposition step. (a) shows the overlay of the (b) germanium and the (c) tin mapping.

4.2.2 Optimisation of the morphology

In chapter 4.2.1 the successful incorporation of tin in the germanium lattice via a kinetically controlled nanowire synthesis was demonstrated. Without pretreatment of the precursor mixture the obtained $Ge_{1-x}Sn_x$ nanowires are not suitable for several applications due to the change of the diameter along the nanowire axis. Pretreatment of the precursor mixture emerged as a viable possibility to optimise the morphology of the $Ge_{1-x}Sn_x$ nanowires.

Pretreatment is realised by the heating of the precursor mixture to 115 °C and stirring overnight at room temperature. The microwave synthesis is performed under identical conditions as the samples without this treatment. The SEM images in figure 14a + c illustrate the homogeneity of the isolated products from this procedure. The morphology of the obtained products depends, as previously described, on the process duration. The TEM image in figure 14b shows nanowires with a constant diameter along their axis. The presence (figure 14d) of an additional terminating segment with diminishing diameter is observed when a long decomposition step is chosen.
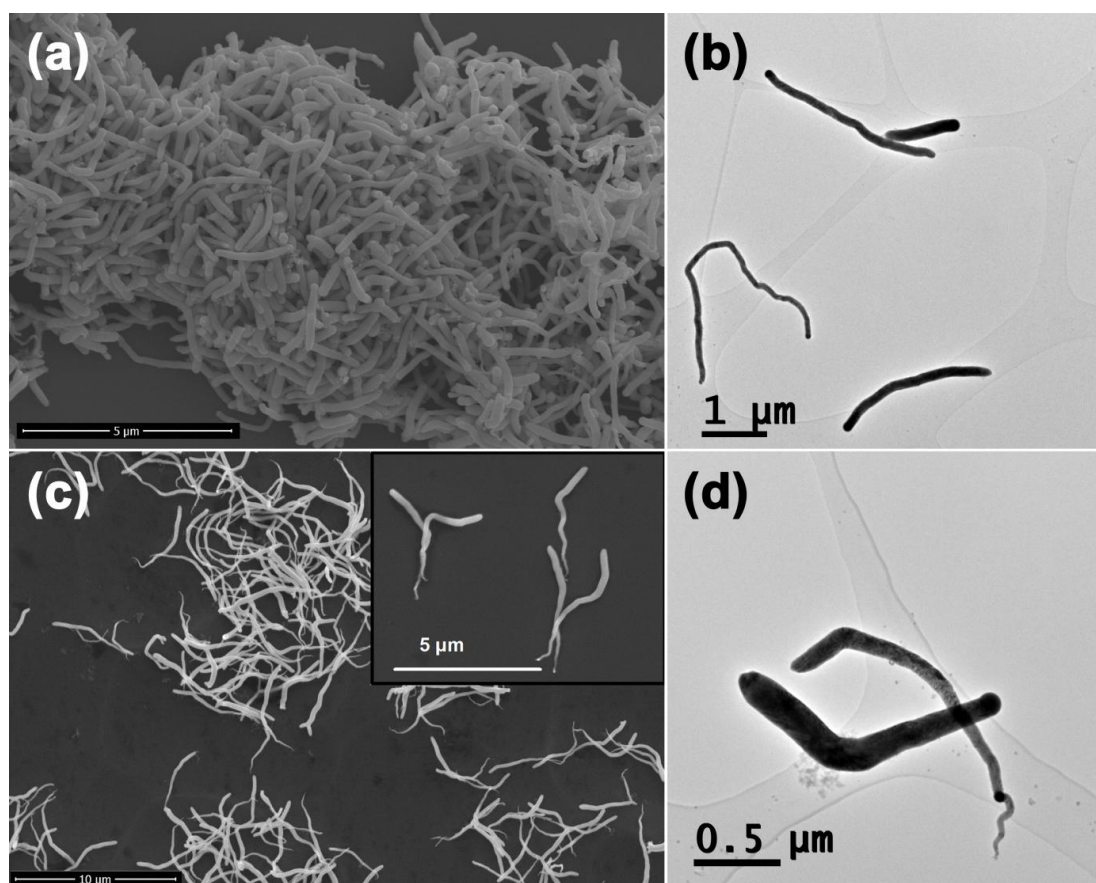
Figure 14: The SEM images in (a) and (c) give an overview of the isolated products from the decomposed precursor mixture for a (a) short and a (c) long decomposition step. The TEM images in (b) and (d) enable a differentiation of the two products in terms of the (b) absence or (d) presence of the segment with diminishing diameter.

The mean diameter of $Ge_{1-x}Sn_x$ nanowires with constant diameter can be determined to 190 ± 30 nm. Compared to the nanowires obtained by the decomposition of a non-pretreated precursor mixture these nanowires are much thicker. EDX elemental mapping images of $Ge_{1-x}Sn_x$ nanowires with constant diameter shown in figure 15 confirm the growth via the SLS mechanism due to the presence of a tin rich nucleus on the growth front. According to the elemental mapping tin is homogeneously distributed in the germanium lattice.
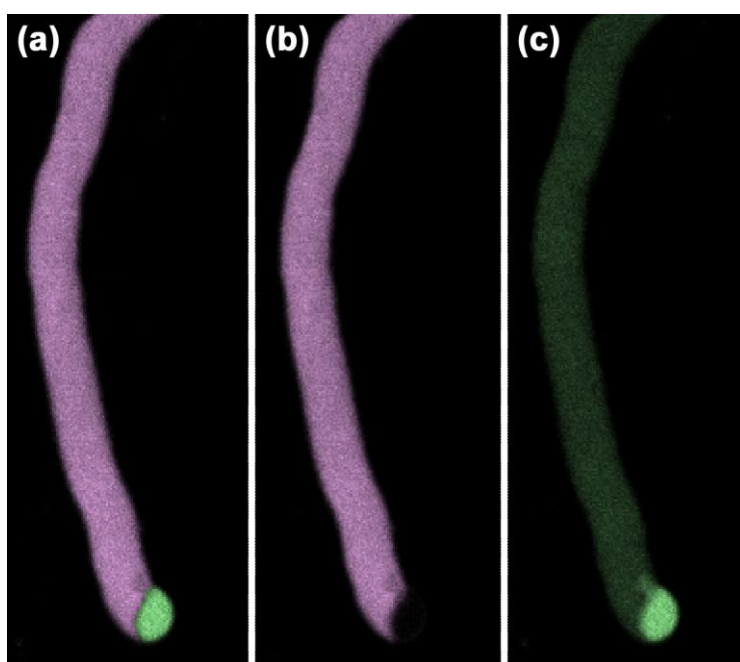

Figure 15: EDX elemental mapping of $Ge_{1-x}Sn_x$ nanowires with a constant diameter. (a) shows the overlay of the (b) germanium and the (c) tin mapping.

The crystallinity is a very important evaluation criterion for the quality of the synthesised $Ge_{1-x}Sn_x$ nanowires. Materials used for photonic or electronic devices need to have a good crystal quality.[15,84-85] HRTEM images of a $Ge_{1-x}Sn_x$ nanowire with constant diameter show high crystallinity with a low number of defects (figure 16a). In general kinking in terms of nanowire growth via the VLS mechanism is often associated to an increased defect density.[106] However, exceptions are known and can be attributed to the growth kinetics.[107] In solution based processes the stirring could disturb the triple phase boundary at the nanowire growth front, which leads to a change of the growth direction. As distinguished from other systems

amines are not known to stabilise a specific crystal facet of germanium, which could explain the change of the growth direction without an accumulation of defects and also the not perfectly smooth side facets of the nanowires. In the HRTEM image of a bent nanowire part shown in figure 16b no increase of the defect density can be observed.
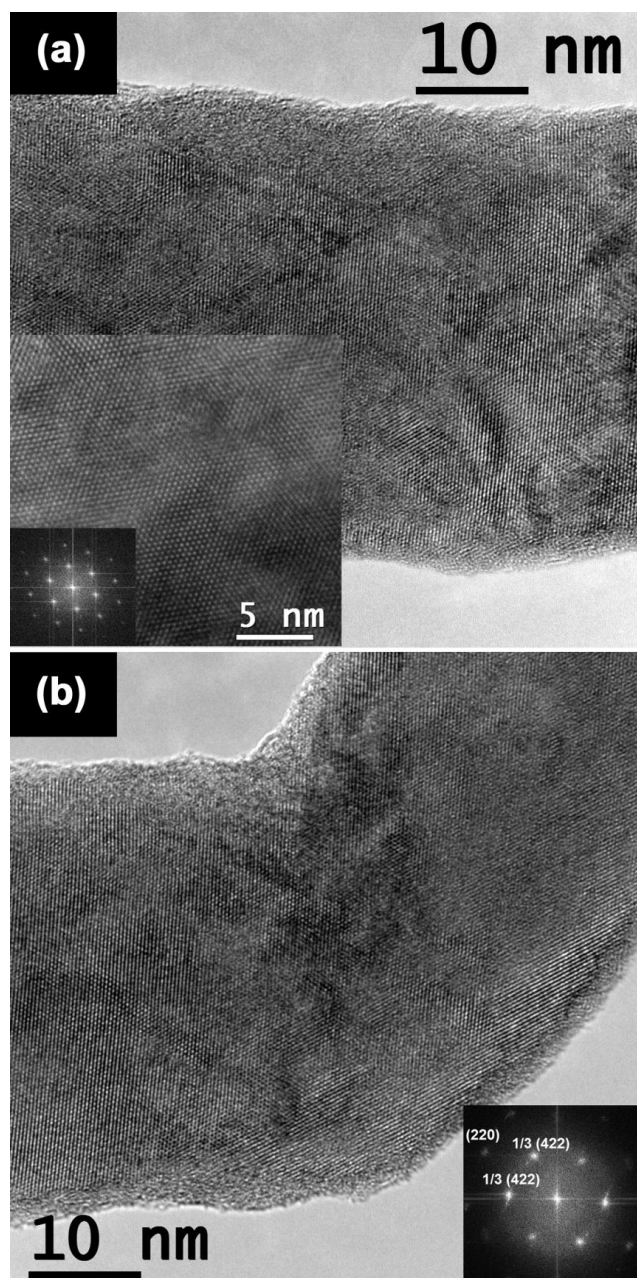
Figure 16: (a) HRTEM image with its corresponding FFT pattern showing the high crystallinity of $Ge_{1-x}Sn_x$ nanowires with constant diameter. (b) HRTEM image of a bent $Ge_{1-x}Sn_x$ nanowire part with its corresponding FFT pattern suggests no increased number of defects.

A further discussion concerning the pseudo hexagonal symmetry of the FFT pattern shown in figure 16 is necessary. For materials crystallised in the diamond structure, which are tilted to the [111] zone-axis orientation, the diffracted beam on the 1/3 (422) position is classically forbidden. The occurrence of these spots can be explained by the small diameter of the nanowires and the increased importance of edge effects for low dimensional structures.[108]

$Ge_{1-x}Sn_x$ nanowires terminated with a diminishing diameter segment show an increased tendency for a change of the growth direction. The HRTEM image collage illustrated in figure 17 points out the high crystallinity of the nanowire segment with diminishing diameter. In this area again no increase of defect density is observable when compared to the nanowire part with constant diameter and the zone axis is retained.
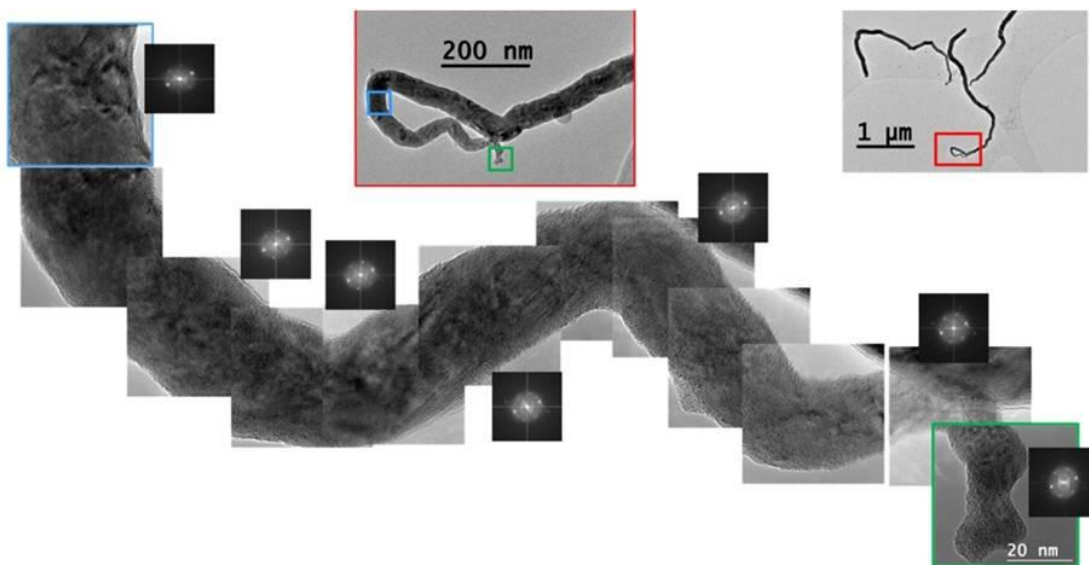
Figure 17: The HRTEM image collage points out the high crystallinity of the segment with diminishing diameter and changes in the growth direction while retaining the zone axis.

Besides crystal defects also metallic tin and amines on the crystal surface can alter the light emission of $Ge_{1-x}Sn_x$.[42,104-105] Grain boundaries and interface states formed by the $Ge_{1-x}Sn_x$ alloy and metallic tin can lead to additional non-radiative recombination sites and therefore a reduced number of radiative recombination

events.[42] The nanowire product contains metallic tin nanoparticles at the tip of the nanowires as already described. The XRD pattern of the as grown $Ge_{1-x}Sn_x$ nanowires in figure 18 clearly shows the presence of the β-tin reflexes. Treatment with diluted hydrochloric acid can be used to purify the $Ge_{1-x}Sn_x$ nanowire material resulting in the disappearance of all the β-tin reflexes. The metallic tin is dissolved and oxidised while the $Ge_{1-x}Sn_x$ nanowire body remains unaffected.
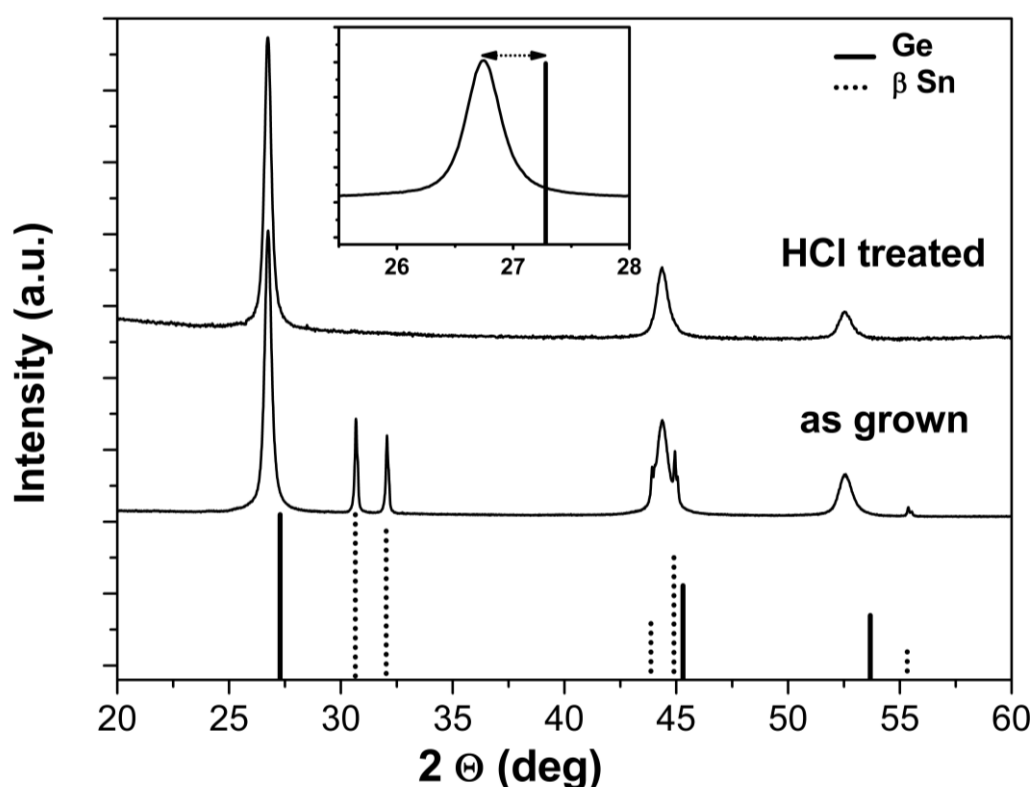
Figure 18: XRD measurements confirm the removal of β-tin. The unaltered shift of the germanium reflex confirms the maintenance of the $Ge_{1-x}Sn_x$ nanowires.

The shift of the germanium reflexes to lower 2θ values can be attributed to the expansion of the germanium lattice when tin is incorporated. The shift can also be used for the determination of the tin content, which will be explained in chapter 4.2.3 in more detail. SEM, TEM and EDX elemental mapping images shown in figure 19 confirm the efficiency of the acid treatment step, the homogeneous distribution of tin in the germanium lattice and the maintenance of the morphology after the treatment with diluted hydrochloric acid.
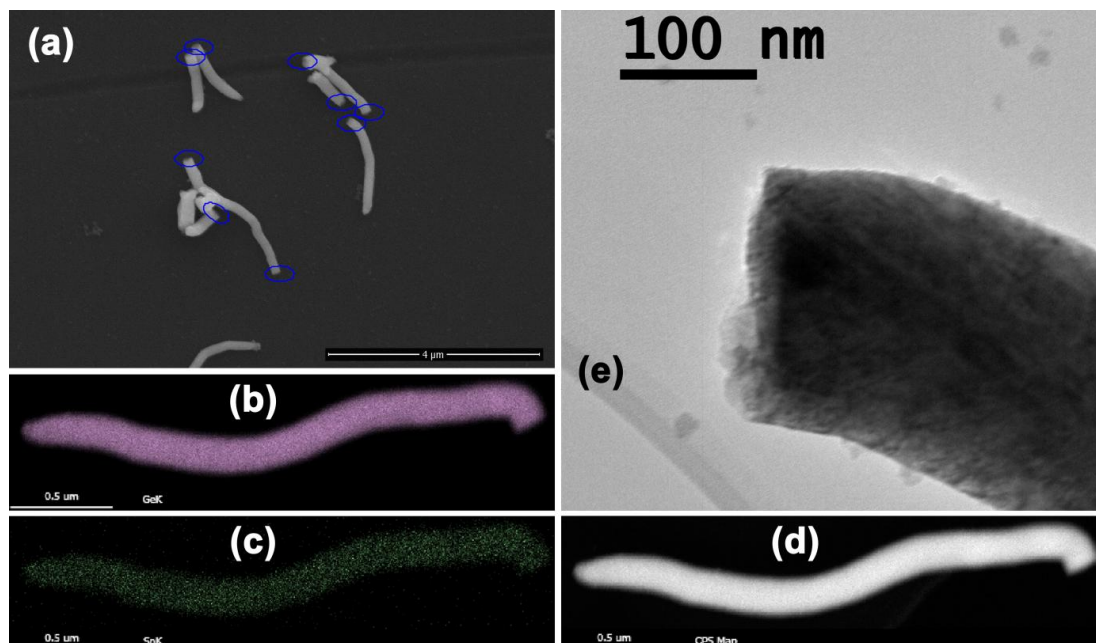
Figure 19: The SEM image (a) shows the successful removal of the tin nucleus on the tip of the $Ge_{1-x}Sn_x$ nanowires. EDX elemental mapping for (b) germanium and (c) tin is done on the $Ge_{1-x}Sn_x$ nanowire which was treated with diluted hydrochloric acid and is shown in the STEM image (d). The absence of the tin nucleus is shown in the TEM image in (e).

4.2.3 Chemical characterisation

The morphology of the $Ge_{1-x}Sn_x$ structures, the quality in terms of the crystallinity and the homogeneous tin distribution in the germanium lattice were already discussed in the previous chapter. In addition to these data the quantitative characterisation concerning the tin content of the $Ge_{1-x}Sn_x$ nanowires is a highly important information. In this study XRD, EDX and Raman spectroscopy (RS) measurements were performed for the determination of the tin content. All of these methods have their advantages and disadvantages. Therefore, a detailed discussion is necessary.

XRD patterns of $Ge_{1-x}Sn_x$ nanowires show two phases before the acid treatment. The tin reflexes show no shift in position when compared to the reference and therefore a shifting of reflexes due to the equipment can be ruled out. $Ge_{1-x}Sn_x$ nanowires with constant diameter are ideal candidates for this method. The method

is a "bulk" characterisation and will average potential variations in the material. The segregation of larger clusters of β-tin inside the nanowire body could be excluded due to the absence of the associated reflexes after the treatment with diluted hydrochloric acid and also their absence in HRTEM images.

In figure 18 the XRD measurement of $Ge_{1-x}Sn_x$ nanowires with constant diameter is shown. Important for the determination of the tin content is the shift of the germanium reflexes, which is attributed to the expansion of the germanium lattice due to the incorporation of tin. Germanium and α-tin are isotype and form a solid solution. For this reason, Vegard's law allows the prediction of the lattice parameter of a certain composition (equation 1). In literature, a correction term for Vegard's law can be found, which is necessary due to the non-linearity of this relation. The theoretically determined correction parameter is called bowing parameter and in good agreement with experimental results obtained from relaxed bulk $Ge_{1-x}Sn_x$.[20,28] According to the experimental results by Gencarelli *et al.* the value 0.041 Å for the bowing parameter *b* is used in this study.[20] The increased importance of surface effects obtained by nanostructured materials could lead to deviations from the real tin content. The tin content is calculated by Vegard's law with and without the correction term (equation 1).

All shifts of the germanium reflexes between the *2θ*-range between 20-90° were used for the calculations. The positions of the germanium reflexes were determined after Rietveld refinement and were then used to calculate the lattice spacing of the corresponding lattice planes. The geometric relations of a cubic system allowed the calculation of the lattice parameter a_{GeSn}. By using the lattice parameters of the pure cubic components (a_{Ge} = 5.658 Å, a_{Sn} = 6.489 Å) an average tin content x_{XRD} was calculated. The results are summarised in table 2.

Table 2: The results of the tin content determination based on XRD data and Vegard's law are summarised.

a_{GeSn} [Å]	b [Å]	x_{XRD} [%]
5.776	-	14.2
5.776	0.041	13.6

Obviously, the bowing parameter has a huge impact on the determination of the tin content. Further methods are necessary to see whether it is valid to involve the used correction of the Vegard's law for nanostructured materials or not.

Therefore, EDX point measurements were performed on a $Ge_{1-x}Sn_x$ nanowire with constant diameter (figure 20). A tin content of 12.1 ± 0.5 % was obtained for these nanowires along the nanowire axis.
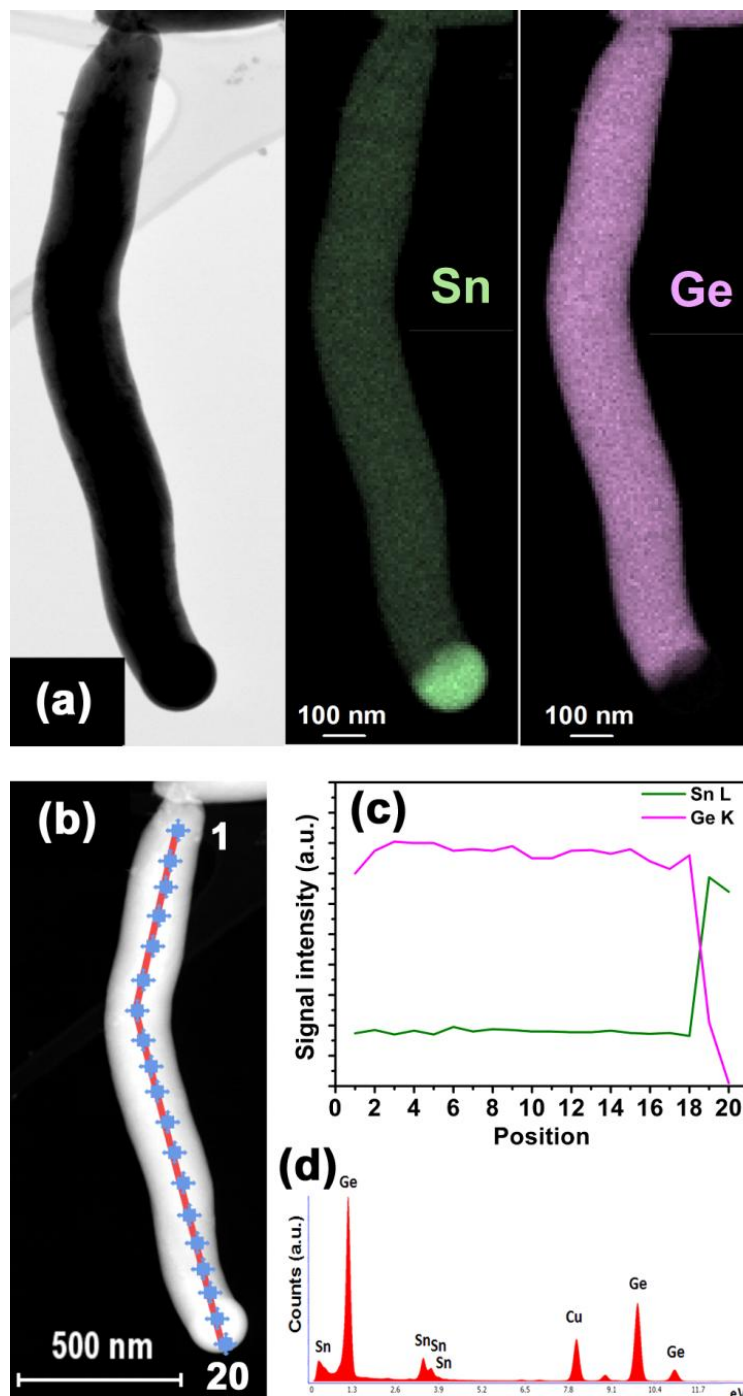
Figure 20: EDX point measurements of a $Ge_{1-x}Sn_x$ nanowire with constant diameter and without the treatment of diluted hydrochloric acid. (a) shows a bright field TEM image of the measured nanowire with the corresponding elemental mapping images of tin and germanium. (b) A high-angle annular dark field (HAADF) image of the nanowire is superimposed with the point EDX locations to obtain the data in (c). The EDX spectrum in (d) is representative of a tin content of 12.1 ± 0.5 %, which is observed in these nanowires.

Additional measurements on acid treated $Ge_{1-x}Sn_x$ nanowires as shown in figure 19b + c were performed. The elemental mapping of tin shown in figure 19c ensures the absence of tin segregation in the nanowire body. The additional results in figure 21 confirm the unaltered tin content of 12.2 ± 0.5 % after the treatment with hydrochloric acid.
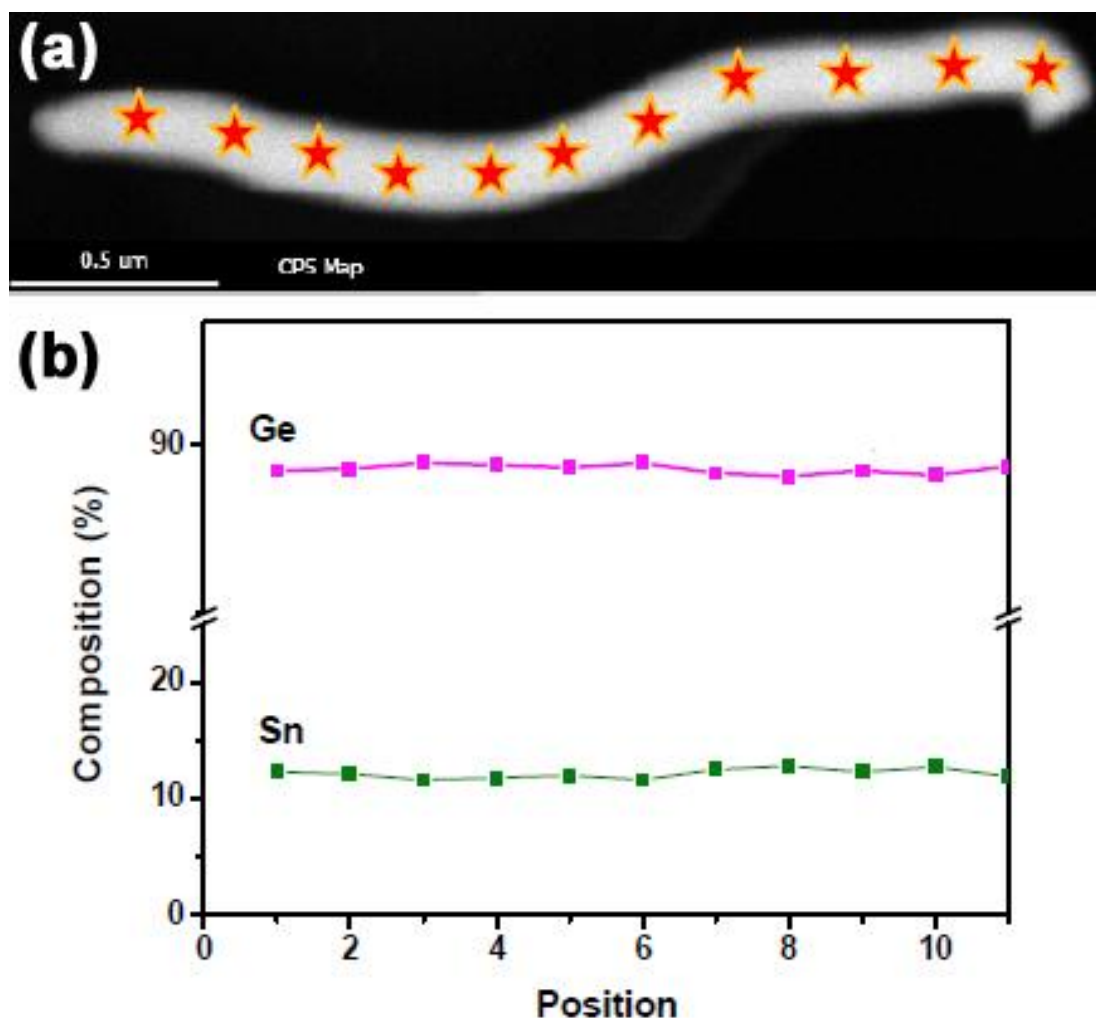
Figure 21: EDX point measurement of a $Ge_{1-x}Sn_x$ nanowire with constant diameter and with the treatment of diluted hydrochloric acid. (a) shows the HAADF image of the nanowire which is superimposed with the point EDX locations to obtain the data in (b). The tin content is constant along the nanowire axis and is determined to 12.2 ± 0.5 %.

The third method used to calculate the tin content in $Ge_{1-x}Sn_x$ is Raman spectroscopy. The magnitude of the Ge-Ge longitudinal optical Raman peak shift difference shows a linear relationship to the tin content of unstrained $Ge_{1-x}Sn_x$ alloys.[109-111] The dependence of the Raman modes on the composition of group 14 alloys can be explained by the sum of mass-disorder and a bond distortion term.[110-113] Also the partially ionic character of the bonds has to be considered.[109,114] The difference of the Raman shifts Δw is equal to the variable z multiplied by the tin content x, where -(82 ± 4) cm^{-1} and -(75.4 ± 4.5) cm^{-1} are the values for the variable z according to literature.[115-116] In equation 2 the relation between the Raman shifts Δw and the tin content x is illustrated.

$$\Delta w = z \cdot x$$

$$\Delta w = \text{difference of the Raman shifts } [\text{cm}^{-1}]$$
$$z = \text{constant of proportionality } [\text{cm}^{-1}]$$
$$x = \text{mole fraction of Sn } [\,]$$

Equation 2: Relationship between the difference of the Raman shifts and the mole fraction is illustrated in this equation.

The requirement of an unstrained $Ge_{1-x}Sn_x$ alloy should be fulfilled in $Ge_{1-x}Sn_x$ nanowires due to the high surface of the nanowires which enables relaxation.[18-19] Besides, no strain-inducing template is used for the synthesis of these nanowires. The low laser power should not lead to a considerable impact of heating effects for nanowires with diameters > 50 nm. In general, the Raman shift of germanium bulk compared to nanowires with a thickness comparable to the one used in this study is essentially the same.[117] In figure 22 the normalised Raman spectra of $Ge_{1-x}Sn_x$ nanowires with constant diameter and germanium nanowires grown via low pressure CVD are shown.[44]
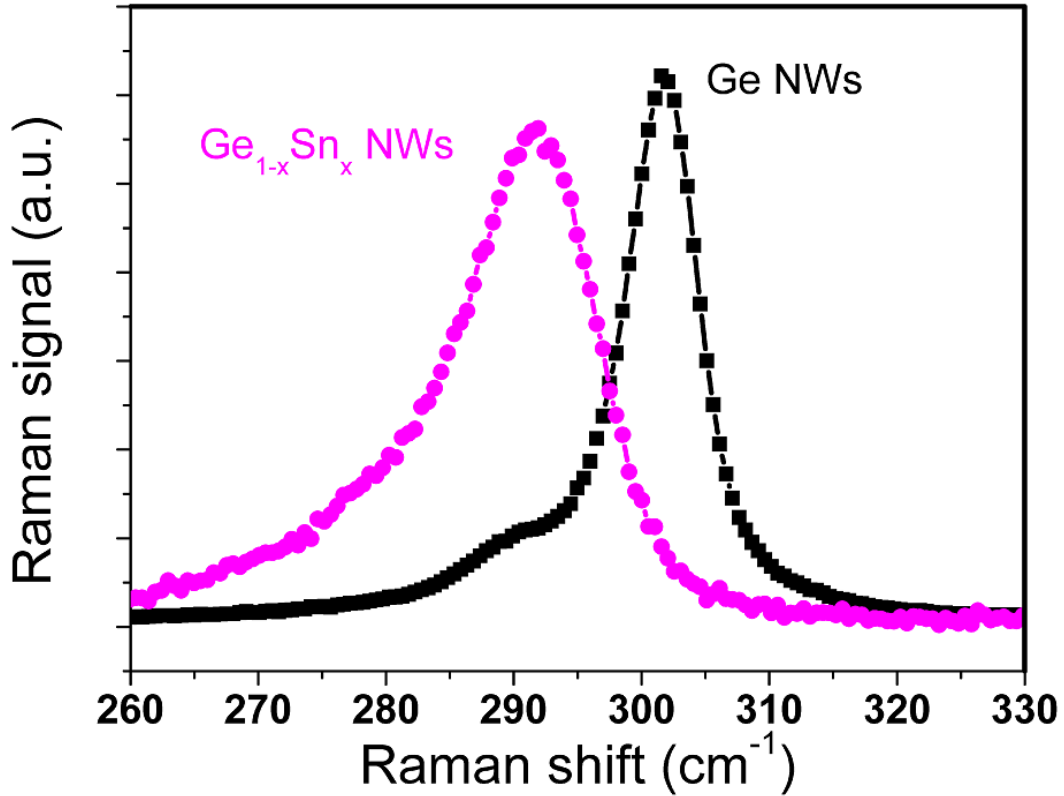
Figure 22: Normalised Raman spectra of $Ge_{1-x}Sn_x$ nanowires with constant diameter and germanium nanowires grown via low pressure CVD. The spectra have been acquired at 532 nm excitation wavelength. The magnitude of the Raman shift difference is determined to -9.9 cm^{-1}.

According to the Raman shift difference of -9.9 cm^{-1} the tin content x_{RS} can be calculated. The errors of the independent variable z are propagated and the results are shown in table 3.

Table 3: The results of the tin content determination based on RS measurements are tabulated.

Δw [cm^{-1}]	z [cm^{-1}]	x [%]	x_{RS} [%]
-9.9	-(82 ± 4)	12.1 ± 0.6	12.6 ± 0.7
-9.9	-(75.4 ± 4.5)	13.1 ± 0.8	

The determined tin content of 12.6 ± 0.7 % based on RS measurements is in good agreement with the results obtained by EDX point measurements. Obviously, the values determined by Vegard's law, which is based on XRD measurements, do not give comparable results. The calculation without the use of the correction term overestimates the tin content while the calculation with the inclusion of the correction term slightly overestimates the tin content. Therefore, only the results obtained by RS and EDX point measurements are used for the calculation of the average tin content x_a. The results are shown in table 4.

Table 4: The results of RS and EDX point measurements are used to calculate the average tin content x_a of the $Ge_{1-x}Sn_x$ nanowires with constant diameter.

x_{EDX} [%]	x_{RS} [%]	x_a [%]
12.1 ± 0.5	12.6 ± 0.7	12.4 ± 0.6

A tin content of 12.4 ± 0.6 % is far above the targeted tin content of 11 %, which was predicted to ensure a transition into a direct band gap material.[2] In addition the used bowing parameter does not seem to describe the relation between the tin content and the lattice parameter properly in the case of $Ge_{1-x}Sn_x$ nanowires. Further results in terms of XRD measurements on $Ge_{1-x}Sn_x$ nanostructures with different tin content could make the calculation of an adapted bowing parameter possible. However, in the first approximation the bowing parameter can be determined by raising the calculated tin content of 12.4 ± 0.6 % and the lattice constant a_{GeSn} of the $Ge_{1-x}Sn_x$ alloy (5.776 Å). As a result the approximated bowing parameter b has a value of 0.138 ± 0.054 Å which is in good agreement with an experimental study by Aella *et al.* where b = 0.166 Å and a theoretical study by Lee *et al.* where b = 0.104.[118]

In addition to the results on constant diameter $Ge_{1-x}Sn_x$ nanowires, individual structures with diminishing nanowire diameter were investigated. EDX point measurements are shown in figure 23. Further shrinkage of the diameter results in a rapid increase of the tin content in the $Ge_{1-x}Sn_x$ alloy. Figure 23e clearly shows the diameter dependent increase of the tin content from 10.7 % for the 270 nm diameter nanowire section up to 28.4 % for the tip region which has a diameter of about 10 nm. In the diameter range 270-100 nm only a slight variation of ~4 % in tin content is recorded. However, values up to 28.4 % tin are observed for the smallest diameters hinting towards a diameter dependent maximum tin content in $Ge_{1-x}Sn_x$. The growth proceeds under a constant tin supply from the tin growth seed. In addition, this tin particle serves as a reservoir of tin for the incorporation and therefore the maximum tin content possible under the given experimental conditions is incorporated in the growing alloy. A viable explanation for the increasing tin content for thinner nanowire diameters can be an efficient strain relaxation at the surface due the high surface-to-volume ratio of one-dimensional structures. According to literature this effect is also responsible for the successful formation of metastable III/V nanowires.[18-19]
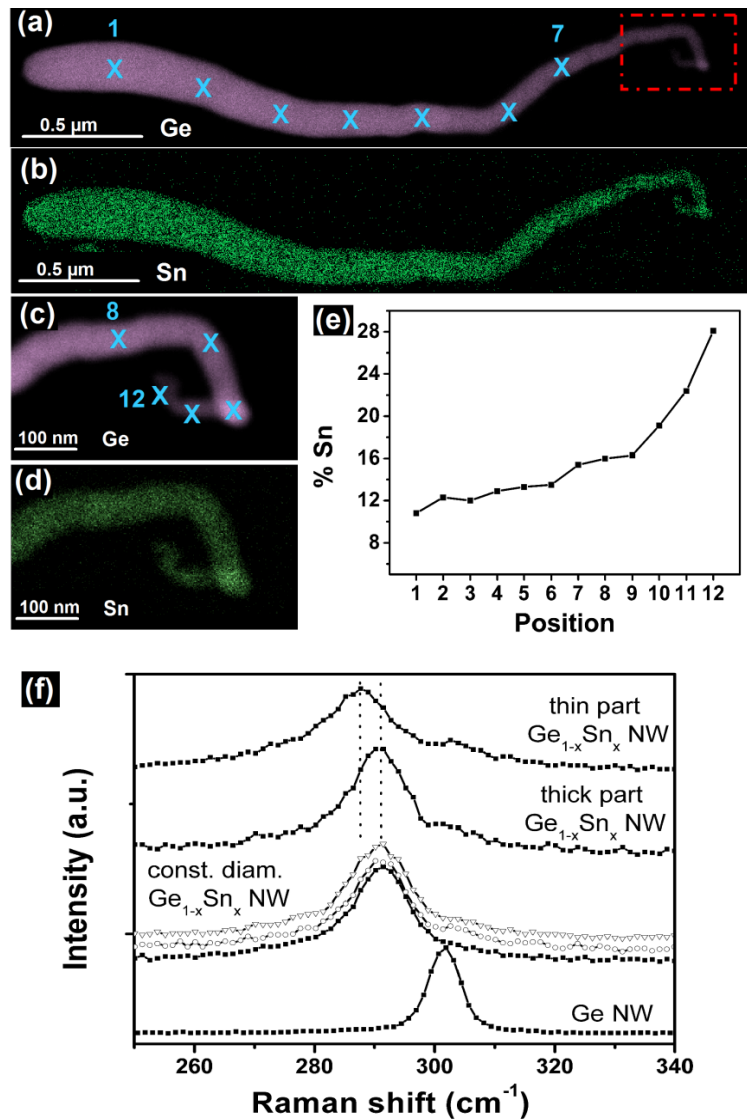
Figure 23: (a) Germanium and (b) tin elemental mapping of a $Ge_{1-x}Sn_x$ nanowire with diminishing diameter obtained after the decomposition of a pretreated precursor mixture. (c) and (d) show the thinner nanowire section marked in (a) which are imaged in a higher magnification to point out the homogeneous distribution of tin in this section and the absence of a tin growth promoter. (e) The point EDX data obtained from the locations illustrated in (a) and (c) show a diameter dependent composition change with diminishing nanowire diameter. (f) A similar change is observed for the Raman signal. A constant nanowire diameter leads to similar spectra at different locations, whereas the signals of the thicker and the thinner part of a nanowire similar to those shown in (a) differ. In addition, the Raman spectrum of a germanium nanowire is shown for comparison. The spectra have been acquired at 532 nm excitation wavelength.

51

These results are supported by µ-Raman measurements. Compared to the Raman signal of the constant diameter $Ge_{1-x}Sn_x$ nanowire region the Raman signal of the tip region is clearly shifted further by an additional 2 cm^{-1} which is equal to 15.5-17.0 % of tin incorporated into the germanium lattice. This is an average of the material in the spot region of the laser beam and the smaller volume of the tip with higher concentration will not contribute much to the obtained spectrum. The results obtained by µ-Raman measurements are limited to the optics which make an accurate positioning of the laser beam complicated. A determination of the corresponding nanowire diameter of the measured region is not possible with the setup used in this study. Heating effects arising from the laser irradiation which could lead to a shift of the Raman signal are excluded for the thicker parts according to literature.[117] The low laser power used in this study should also avoid the influence of heating effects for the tip region. Apart from the here described alloying, a shift of the Raman signal can also occur for strained structures. For nanowires these effects should be absent due to the benefited strain relaxation[19] in contrast to thin $Ge_{1-x}Sn_x$ films where substrate effects[119] can lead to a shift of the Raman signal.

The diameter dependent composition change with diminishing diameter is a very important finding in terms of the improvement of the $Ge_{1-x}Sn_x$ nanowires synthesised in this study. The synthesis of thinner $Ge_{1-x}Sn_x$ nanowires in a kinetically controlled process should yield a higher tin content. Furthermore, the controlled synthesis concerning the nanowire diameter could enable the adjustment of the band gap.

4.3 Model of the growth mechanism

The understanding of the growth mechanism is a very important part to complete this study. Pretreatment of the precursor mixture turned out to be the key step for the synthesis of $Ge_{1-x}Sn_x$ nanowires with constant diameter. Attempts to decipher the processes occurring during the decomposition of the precursor mixture are presented in this chapter.

Three regimes can be obtained according to the products shown in figure 12 for the decomposition of the precursor mixture without a pretreatment step. Depending on the duration of the decomposition different morphologies can be observed. A short decomposition step leads to $Ge_{1-x}Sn_x$ nanowires with expanding diameter. If the decomposition step is extended subsequent to the expanding segment a further segment with constant diameter can be observed. A long decomposition step yields a segment with diminishing diameter in addition to the already discussed segments. The chosen process is kinetically controlled, which implies a huge impact of the availability of the components. The comparison of the bond energies of Ge-N and Sn-N, where the Sn-N bond is slightly weaker, allows the conclusion that the decomposition rate of the tin rich imido cubanes is higher than the decomposition rate of the germanium rich imido cubanes at 230 °C.[120]

The heating of the precursor mixture without pretreatment starts with the formation of tin nanoparticles due to the predominant thermal decomposition of the homometallic tin imido cubanes accompanied with heterometallic tin rich imido cubanes. Germanium supersaturates the tin nanoparticles very quickly and germanium nuclei are formed. The supplied amount of tin exceeds the limit which can be incorporated into the germanium lattice at this stage. As a result the molten tin particles are expanding during the elongation of the $Ge_{1-x}Sn_x$ nanowires. This also serves as an explanation of the expanding diameter of this segment. An example of this growth regime with expanding nanowire diameter is shown in figure 12a.

After the so called nucleation regime the conditions in the precursor mixture change in favour of the heterometallic germanium rich imido cubanes. The supplied Ge/Sn ratio is then dominated by this species where the amount of tin can nearly be incorporated into the germanium lattice. In addition, the homometallic germanium imido cubanes are decomposing and provide germanium for crystal growth. Further expansion of the tin particles is not expected in the elongation regime. As a result a segment of constant diameter is produced. Figure 12b provides images of this growth regime.

At the point where only homometallic germanium imido cubanes are available in the precursor mixture tin cannot be supplied any longer. The prolonged supply of germanium leads to further growth of the $Ge_{1-x}Sn_x$ nanowires. The incorporation of tin into the germanium lattice continues and leads to a segment with diminishing

diameter due to the consumption of the tin particle. The termination regime yields nanowires as shown in figure 12c.

The pretreatment of the precursor mixture has a significant effect. For the clarification of the growth mechanism which occurs during the decomposition of a pretreated precursor mixture TEM images of the initial part (figure 24) are important. It is obvious that often small structures or surface roughness can be found at the initial site of $Ge_{1-x}Sn_x$ nucleation. Moderate sonication does not remove the small structures (figure 24a-c) while an intense sonication step leads to surface roughness (figure 24d + e). A closer look on the orientation of the small crystallites by investigating FFT patterns of the desired areas suggests the appearance of an effective oriented attachment process during the nucleation regime. Hobbs *et al.* suggested a similar process for the extension and growth of seed-free germanium nanowires.[121] Besides these findings it has to be considered that the $Ge_{1-x}Sn_x$ nanowires, which are produced by the decomposition of a non-pretreated and a pretreated precursor mixture, differ in the average diameter. At this stage of the investigations, $Ge_{1-x}Sn_x$ nanowires with constant diameter are much thicker.
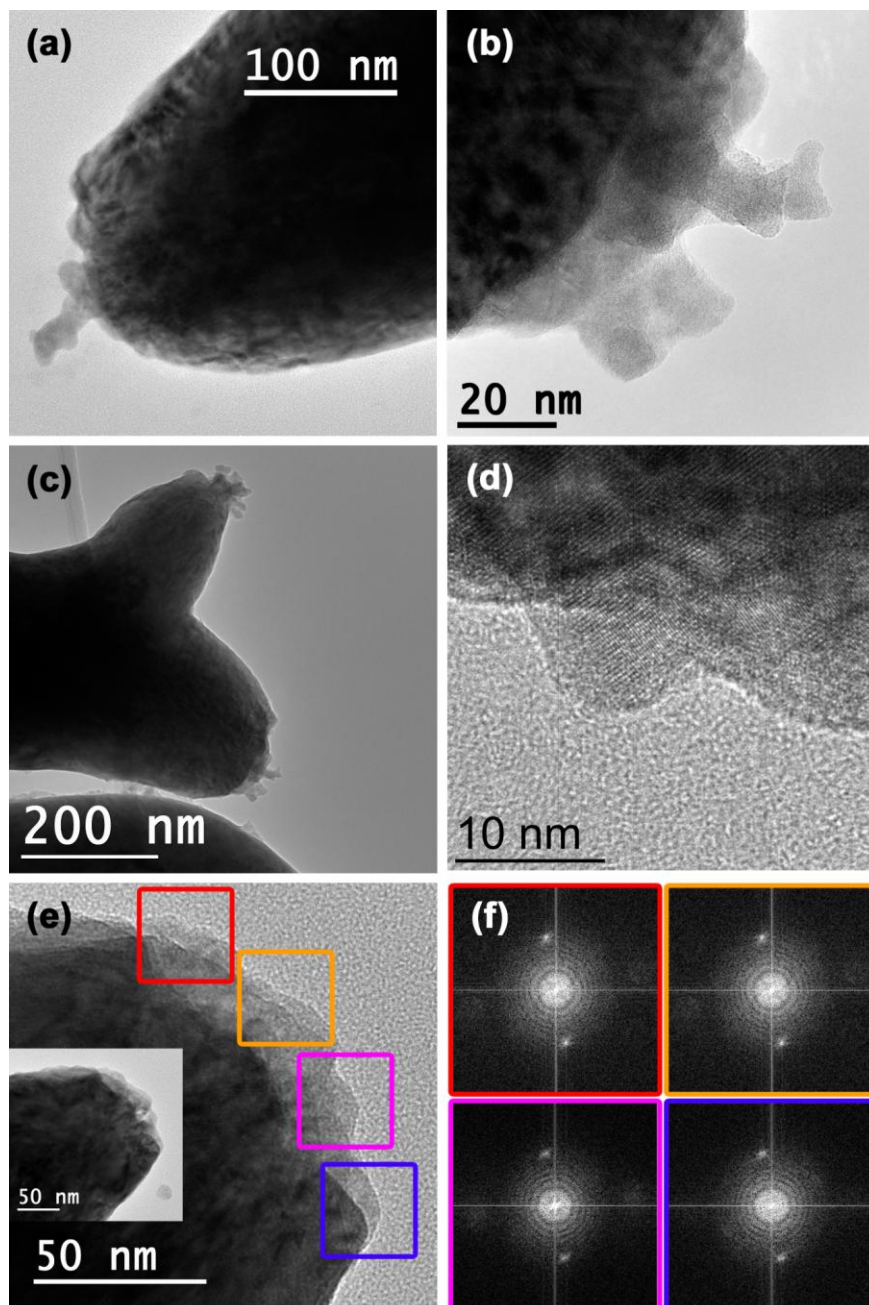
Figure 24: The TEM images reveal the state of the initial nucleation after heating the pretreated precursor mixture. The images in (a-c) illustrate the initial crystallites remaining at the nucleation site after moderate sonication. Most of the small crystallites are removed after the sonication step which is used during the cleaning procedure. (d + e) The TEM images with all the initial particles detached causing a rough surface. The initial nucleation can be associated with an oriented attachment which is supported by the FFT patterns in (f) from different locations of the rough surface where the initial nanocrystals are broken off in (e). The same orientation of the crystallites/segments forming the rough surface is an indication for the oriented attachment.

Putting all these findings together oriented attachment seems to be a plausible explanation for the nucleation of thicker nanowires. In theory the pretreatment of the precursor mixture leads to the formation of initial tin particles and the depletion of tin rich imido cubanes in the mixture. This process is most probably accompanied by the formation of $Sn/Ge_{1-x}Sn_x$ heterodimers. Tin particles are weakly stabilised by the amines and therefore they can partly agglomerate during the heating up step in the microwave synthesis. The agglomerated tin particles fuse together very quickly after reaching the melting point to minimise the surface free energy. The decomposition step leads to the fast supersaturation of single tin particles which are still present in the mixture due to the predominant thermal decomposition of the heterometallic germanium imido cubanes. Simultaneously, the single tin particles which partly contain a growing $Ge_{1-x}Sn_x$ nucleus fuse together with the bigger tin particles. The driving force is again the minimisation of the surface free energy. The $Ge_{1-x}Sn_x$ nuclei from the heterodimers can move unrestricted on the surface of the big tin particles where they arrange and fuse together to minimise the surface free energy, forming a bigger $Ge_{1-x}Sn_x$ crystal. This step is called oriented attachment. The schematic illustration shown in figure 25 visualises the steps occurring during the nucleation regime of $Ge_{1-x}Sn_x$ nanowires with constant diameter.
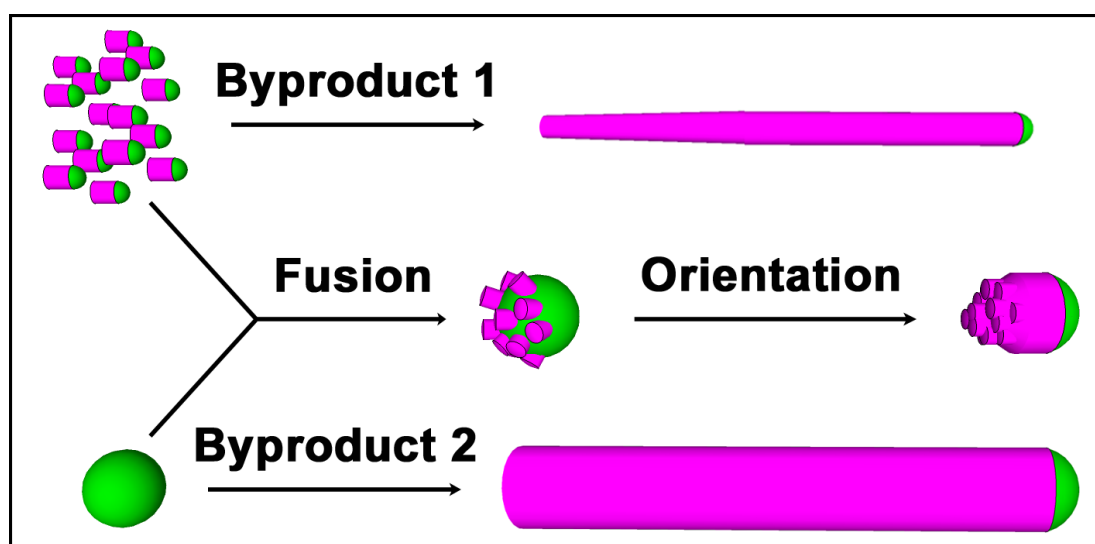
Figure 25: Schematic illustration representing the steps occurring during the nucleation regime of $Ge_{1-x}Sn_x$ nanowires with constant diameter.

However, this process is most likely not the exclusive event in the reaction mixture concerning nucleation and growth. A small fraction of $Ge_{1-x}Sn_x$ nanowires with thin diameters can be observed, which could be resulting from the elongation of the initially built $Sn/Ge_{1-x}Sn_x$ heterodimers. Moreover, the smooth initial part observed for a couple of $Ge_{1-x}Sn_x$ nanowires with thick diameters suggests the absence of oriented attachment. In this case the bigger tin particles in the precursor mixture become supersaturated during the nucleation regime and grow via the SLS mechanism from a single nucleus which is quickly expanding.

The weak stabilisation of the molten tin particle leads to the possibility of a fusion of $Ge_{1-x}Sn_x$ nanowires even after the nucleation regime. Compared to the nucleation regime the probability for such a fusion event is decreased in the elongation regime due to the lower probability of a contact between the molten growth seeds. However, small amounts of the structures shown in figure 26 can be observed in the isolated product.
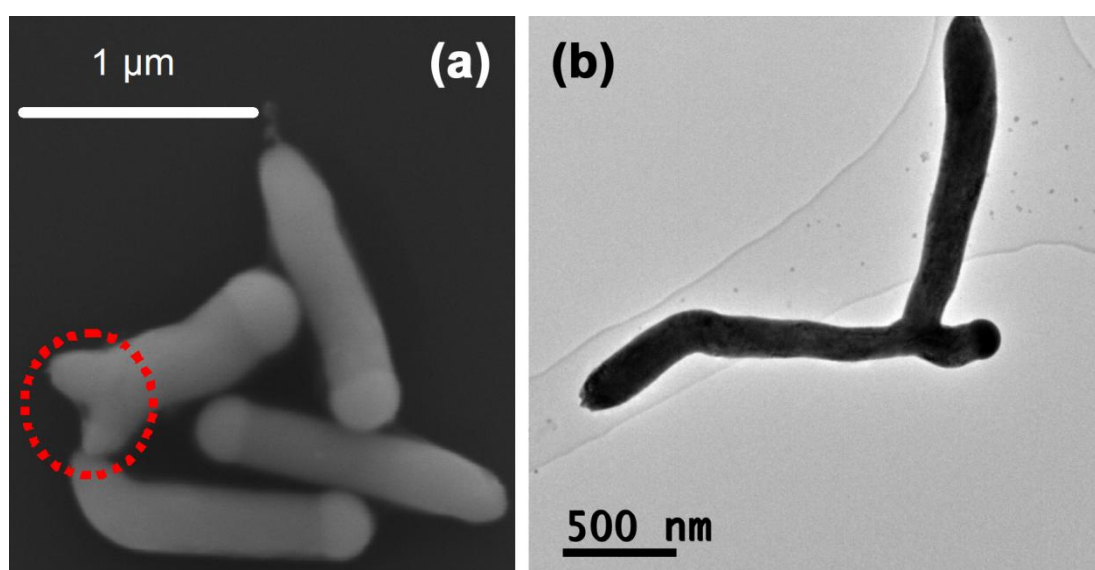
Figure 26: Fused $Ge_{1-x}Sn_x$ nanowires are shown in this figure. The fusion event of two $Ge_{1-x}Sn_x$ nanowires can occur (a) very early or (b) at a later point in the elongation regime.

Depending on the point where the fusion event takes place during the elongation step different structures, which are shown in figure 26, can be observed.

Also some indications for an oriented attachment process for $Ge_{1-x}Sn_x$ nanowires produced without the pretreatment of the precursor mixture could be found. In figure 27 a HRTEM image shows an area where a sudden diameter expansion can be observed. The formed twin could be caused by an oriented attachment event in the nucleation/elongation regime of this nanowire.
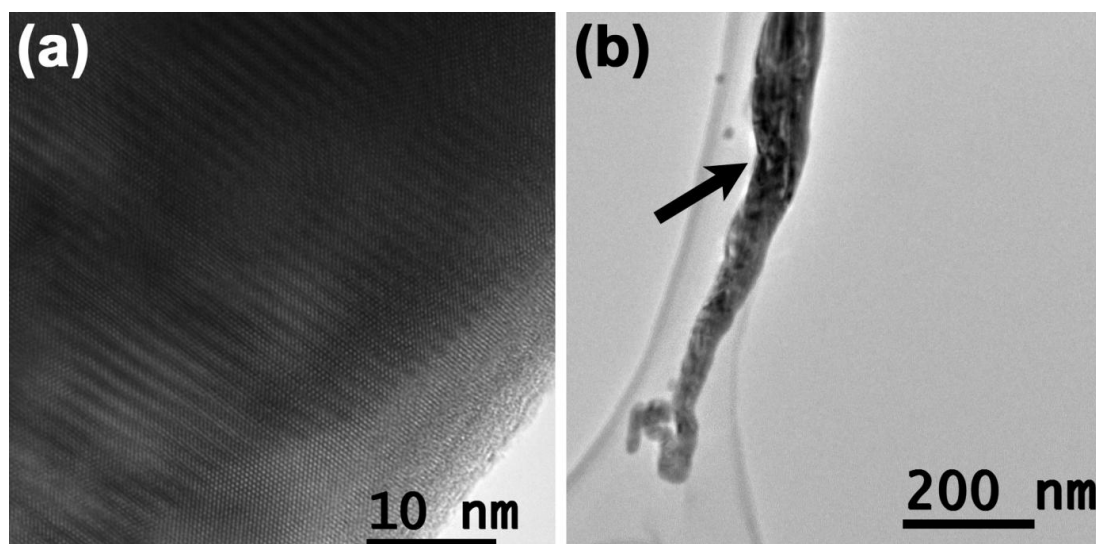
Figure 27: The HRTEM image in (a) shows an area of a $Ge_{1-x}Sn_x$ nanowire produced by the decomposition of a non-pretreated precursor mixture where a Moiré pattern which indicates a twin is clearly visible. The location of this area is shown in the TEM image in (b) and is accompanied by a sudden diameter expansion.

All the findings concerning the growth mechanism are summarised in figure 28. The schematic overview differentiates whether pretreatment of the precursor mixture is performed or not and separates the growth into three regimes. These regimes can be attributed to a specific nanowire segment observed. In theory a controlled synthesis allows the production of specific nanowire segments by manipulating the supplied Ge/Sn ratio.
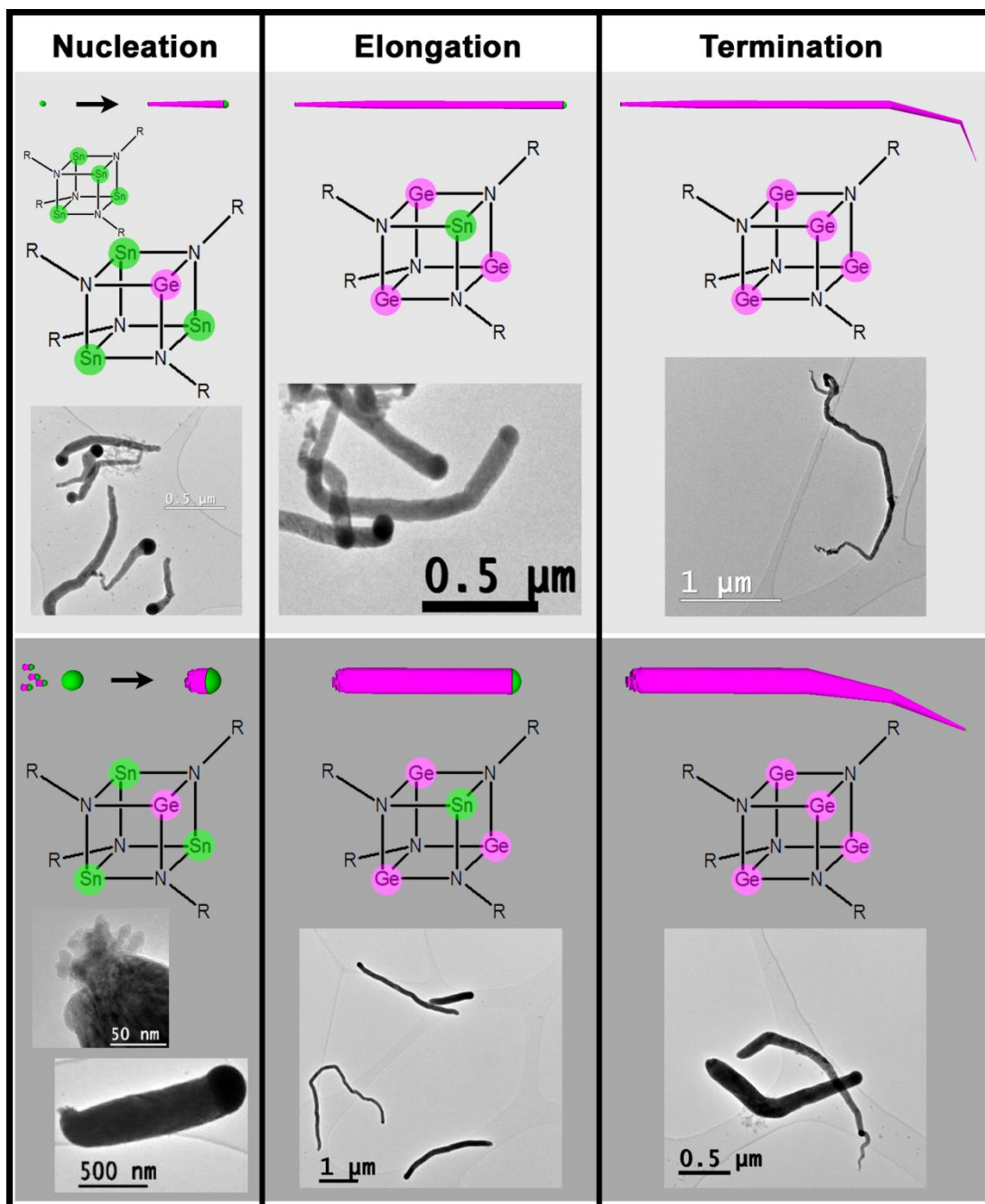
Figure 28: Summary of the growth regimes observed for the decomposition of a non-pretreated (light gray) and a pretreated (dark gray) precursor mixture. The growth can be separated into the nucleation, the elongation and the termination regime. The characteristic $Ge_{1-x}Sn_x$ nanowire morphology of each stage is illustrated by an attached TEM image.

5 Summary

This study represents the first controlled bottom-up synthesis of $Ge_{1-x}Sn_x$ nanowires with a constant diameter of 190 ± 30 nm and a high tin content of 12.4 ± 0.6 % in a microwave-assisted process. The thermodynamically controlled solid solubility of tin in germanium is far below the content which enables the transition to a direct band gap material. Therefore, a kinetically controlled process at low temperatures is developed. For a kinetically controlled process the control of the supplied species is critical. Consequently, the precursor plays a key role in this work. Homo- and heterometallic imido cubanes are identified and used as precursors in the synthesis of $Ge_{1-x}Sn_x$ nanostructures for the first time.

The ratio of the imido cubanes, the pretreatment of the precursor mixture and the low temperatures are identified as the main reasons for the successful synthesis of $Ge_{1-x}Sn_x$ nanowires with constant diameter and a high tin content. Increasing and diminishing nanowire diameters are related to the presence of specific precursor species. The growth regimes described in this study are dependent on the availability and decomposition of specific imido cubane derivatives with different Ge/Sn ratio.

The homogenous distribution of tin in the germanium lattice of the highly crystalline $Ge_{1-x}Sn_x$ alloys is verified by EDX elemental mapping. The tin content is determined by complementary techniques, such as XRD, Raman and EDX analysis. Raising the shifts of the reflexes in the XRD pattern to calculate the tin content by using Vegard's law, a bowing parameter is needed for the correction of the occurring overestimation. The results from Raman and EDX measurements allow the estimation of the bowing parameter for $Ge_{1-x}Sn_x$ nanowires, which is in good agreement with values known from $Ge_{1-x}Sn_x$ thin films. The tin content of $Ge_{1-x}Sn_x$ nanowires increases with reduced nanowire diameter, which is verified by EDX and μ-Raman analysis.

The growth regimes are identified by comparing electron microscopy images. A modification of the experimental procedure allows the growth of $Ge_{1-x}Sn_x$ nanowires with constant diameter, which seems to be dependent on an oriented attachment in the nucleation regime. According to these findings, a model for the

growth regimes is suggested relating the available precursor species to the growing $Ge_{1-x}Sn_x$ nanostructure.

6 Experimental

6.1 Precursor synthesis

Butyl lithium, hexamethyldisilazane, tin(II) chloride, 1,1,3,3-tetramethyldisiloxane and germanium(IV) chloride were purchased from Sigma-Aldrich. All solvents were dried by standard procedures and stored under molecular sieve. Lithium bis(trimethylsilyl)amide was prepared by a chemical reaction of butyl lithium and hexamethyldisilazane in dry hexane.[122] The obtained colourless solid was purified by sublimation under reduced pressure. The germanium(II) chloride dioxane complex was synthesised according to a published procedure.[123]

The synthesis of bis[bis(trimethylsilyl)amino]tin(II) was prepared by a modified procedure published by Lappert *et al.* where 2 equivalents of lithium bis(trimethylsilyl)amide are dissolved in dry tetrahydrofuran and are then added to a solution of 1 equivalent of anhydrous tin(II) chloride in dry tetrahydrofuran.[124] During the addition of the lithium bis(trimethylsilyl)amide solution the reaction mixture became warm and turned red-orange in colour. The reaction mixture was refluxed for 2 h followed by the replacement of the solvent by dry toluene and the removal of lithium chloride. The solvent was removed under reduced pressure and the residue was purified by vacuum distillation. The product was collected as bright red oil in 85 % yield.

A similar procedure was used to synthesise bis[bis(trimethylsilyl)amino]germanium(II) from the prepared germanium(II) chloride dioxane complex. The orange amide was isolated by distillation under reduced pressure in 66 % yield.

Dodecylamine (98 %) was kept at 60 °C for 2 h under dynamic vacuum and was distilled afterwards under reduced pressure. The obtained distillate was colourless and free of solid particles.

The homometallic imido cubanes as well as mixed imido cubane species were investigated via NMR techniques. The homometallic imido cubanes were prepared in the glove box by mixing 1 part of the metal amide with approx. 1 part of

dodecylamine in dry benzene to enable effective stirring. The mixture was stirred for 5 h at 50 °C. Subsequently, benzene and hexamethyldisilazane were removed under reduced pressure. The synthesis of the mixed imido cubane species was performed analogous to the preparation of the homometallic imido cubanes with the difference of mixing 1 part of bis[bis(trimethylsilyl)amino]tin(II), 4 parts of bis[bis(trimethylsilyl) amino]germanium(II) and approx. 5 parts of dodecylamine in dry benzene. The homometallic tin imido cubane solidified quickly whereas the mixed imido cubane species and the homometallic germanium imido cubane remained a viscous liquid. The residues were dissolved in deuterated benzene for the characterisation via NMR.

6.2 Materials synthesis

$Ge_{1-x}Sn_x$ nanowires were grown in 10 ml glass cells (Anton Paar GmbH) at temperatures between 230-240 ºC. The handling of the chemicals as well as the filling of the reaction vessels was carried out in a glove box under stringent precautions against water. A stock solution of 8 mM bis[bis(trimethylsilyl)amino]tin(II) and 32 mM bis[bis(trimethylsilyl)amino]germanium(II) in dodecylamine was prepared. This solution was stirred for 12 h at room temperature to ensure the formation of the metal imides which is accompanied with a colour change to a bright orange. In a typical experiment 3 ml of the dodecylamine stock solution were transferred into a glass cell for microwave synthesis and sealed with a Teflon coated rubber cap. This vial was then transferred to the microwave reactor (Monowave 300; Anton Paar GmbH; wavelength 2.46 GHz) with an IR temperature control unit. The solution was heated as quickly as possible to 230 °C (~3.5 min). The temperature was held for 1-30 min at the desired temperature and was cooled down by a gas stream. The nanowires were collected by adding toluene (3 ml) and centrifugation. The collected solid material was redispersed in toluene and centrifuged again to remove the dodecylamine. In total this step was repeated five times. The product was stored under ambient conditions in toluene. Pretreatment of the precursor mixture was achieved by heating it to 115 °C on a hotplate with vigorous stirring and immediate removal from the heat source when the temperature was reached. The stock solution was cooled down to room temperature and aged overnight before the actual

microwave synthesis was performed as described above. After stirring the pretreated precursor mixture overnight the content looks cloudy but moderate heating results in a clear light orange solution. According to figure 28 the experimental data to produce the obtained products are presented in table 5.

Table 5: Experimental data for the synthesis of the specific products shown in figure 28.

	pretreatment	decomposition step [min]	Ge:Sn
nucleation	no	1-5	4:1
	yes	< 1	4:1
elongation	no	5-15	4:1
	yes	1-5	4:1
termination	no	15-30	4-5:1
	yes	5-15	4.5-5:1

Subsequently, the purification of the product can be carried out by the treatment in 10 % hydrochloric acid for 10 min.

6.3 Characterisation

^{1}H solution NMR spectra were recorded on a Bruker AVANCE 250 spectrometer (250.13 MHz {^{1}H}) equipped with a 5 mm inverse-broadband probe head and a *z*-gradient unit. Deuterated benzene (C_6D_6) was purchased from Euriso-top and stored over molecular sieve (4 Å).

The $Ge_{1-x}Sn_x$ nanowires were analysed using a FEI Quanta 200 SEM. The $Ge_{1-x}Sn_x$ nanowires were deposited on lacey carbon and carbon film copper grids for TEM characterisation (Plano). In this study, a FEI TECNAI F20 operated at 200 kV and equipped with high-angle annular dark field STEM and EDX detector was used. The elemental maps were recorded using the AMETEK TEAM package. The images were recorded and treated using Digital Micrograph software. The XRD patterns were recorded on a PANalytical X-Pert PRO PW 3050/60 in Bragg-Brentano geometry and Cu-Kα radiation. The Rietveld refinement was carried out using X-pert Highscore software.

The Raman spectra shown in figure 22 were acquired using a Horiba LabRam 800 HR with a laser power of 200 µW and a wavelength of 532 nm. The µ-Raman measurements shown in figure 23 were performed on a WITec alpha300 Raman system with a frequency-doubled Nd:YAG laser (λ = 532 nm) in a backscattering geometry. The nanowires were dispersed on a Si substrate and positioned via a xyz piezo-stage by imaging the surface through a microscope with a CCD. The power of the incident laser was adjusted to 150 µW, which should be low enough to exclude modification of the nanowire and heating effects.[117]

7 Literature

1.   S. Gupta, B. Magyari-Köpe, Y. Nishi, K. C. Saraswat, *Journal of Applied Physics* **2013,** *113*, 073707.

2.   K. Lu Low, Y. Yang, G. Han, W. Fan, Y.-C. Yeo, *Journal of Applied Physics* **2012,** *112*, 103715.

3.   W. Huang, B. Cheng, C. Xue, C. Li, *Physica B: Condensed Matter* **2014,** *443*, 43-48.

4.   E. Kasper, M. Kittler, M. Oehme, T. Arguirov, *Photonics Research* **2013,** *1*, 69-76.

5.   E. Kasper, J. Werner, M. Oehme, S. Escoubas, N. Burle, J. Schulze, *Thin Solid Films* **2012,** *520*, 3195-3200.

6.   J. Fan, P. K. Chu, *Small* **2010,** *6*, 2080-2098.

7.   D. Klimm, *IUCrJ* **2014,** *1*, 281-290.

8.   A. Hirsch, *Nat Mater* **2010,** *9*, 868-871.

9.   H. I. T. Hauge, M. A. Verheijen, S. Conesa-Boj, T. Etzelstorfer, M. Watzinger, D. Kriegner, I. Zardo, C. Fasolato, F. Capitani, P. Postorino, S. Kölling, A. Li, S. Assali, J. Stangl, E. P. a. M. Bakkers, *Nano Letters* **2015,** *15*, 5855-5860.

10.   Z. Zhao, F. Tian, X. Dong, Q. Li, Q. Wang, H. Wang, X. Zhong, B. Xu, D. Yu, J. He, H.-T. Wang, Y. Ma, Y. Tian, *Journal of the American Chemical Society* **2012,** *134*, 12362-12365.

11.   L. Vincent, G. Patriarche, G. Hallais, C. Renard, C. Gardès, D. Troadec, D. Bouchier, *Nano Letters* **2014,** *14*, 4828-4836.

12.   S. Küfner, J. Furthmüller, L. Matthes, M. Fitzner, F. Bechstedt, *Physical Review B* **2013,** *87*, 235307.

13.   R. W. Olesinski, G. J. Abbaschian, *Bulletin of Alloy Phase Diagrams* **1984,** *5*, 180-183.

14.   S. Wirths, R. Geiger, N. Von Den Driesch, G. Mussler, T. Stoica, S. Mantl, Z. Ikonic, M. Luysberg, S. Chiussi, J. M. Hartmann, H. Sigg, J. Faist, D. Buca, D. Grützmacher, *Nat Photon* **2015,** *9*, 88-92.

15.   H. Genquan, S. Shaojian, Z. Chunlei, Z. Qian, Y. Yue, W. Lanxiang, G. Pengfei, W. Wang, W. Choun Pei, S. Ze Xiang, C. Buwen, Y. Yee-Chia In *High-mobility germanium-tin (GeSn) P-channel MOSFETs featuring metallic source/drain and sub-370 °C process modules*, Electron Devices Meeting (IEDM), 2011 IEEE International, 5-7 Dec. 2011; 2011; pp 16.7.1-16.7.3.

16.   R. W. Olesinski, G. J. Abbaschian, *Bulletin of Alloy Phase Diagrams* **1984,** *5*, 265-271.

17.   J. D. Sau, M. L. Cohen, *Physical Review B* **2007,** *75*, 045208.

18.   E. Ertekin, P. A. Greaney, D. C. Chrzan, T. D. Sands, *Journal of Applied Physics* **2005,** *97*, 114325.

19.   T. Kuykendall, P. Ulrich, S. Aloni, P. Yang, *Nat Mater* **2007,** *6*, 951-956.

20.   F. Gencarelli, B. Vincent, J. Demeulemeester, A. Vantomme, A. Moussa, A. Franquet, A. Kumar, H. Bender, J. Meersschaut, W. Vandervorst, R. Loo, M. Caymax, K. Temst, M. Heyns, *ECS Journal of Solid State Science and Technology* **2013,** *2*, P134-P137.

21.   M. Bauer, J. Taraci, J. Tolle, A. V. G. Chizmeshya, S. Zollner, D. J. Smith, J. Menendez, C. Hu, J. Kouvetakis, *Applied Physics Letters* **2002,** *81*, 2992-2994.

22.   G. Grzybowski, R. T. Beeler, L. Jiang, D. J. Smith, J. Kouvetakis, J. Menéndez, *Applied Physics Letters* **2012,** *101*, 072105.

23.   C. I. Ventura, J. D. Fuhr, R. A. Barrio, *Physica B: Condensed Matter* **2009,** *404*, 2830-2833.

24.   L. Vegard, *Zeitschrift für Physik* **1921,** *5*, 17-26.

25.   H. W. King, *Journal of Materials Science* **1966,** *1*, 79-90.

26.   H. J. Axon, W. Hume-Rothery, *Proceedings of the Royal Society of London A: Mathematical, Physical and Engineering Sciences* **1948,** *193*, 1-24.

27.   A. R. Denton, N. W. Ashcroft, *Physical Review A* **1991,** *43*, 3161-3164.

28.   R. Beeler, R. Roucka, A. V. G. Chizmeshya, J. Kouvetakis, J. Menéndez, *Physical Review B* **2011,** *84*, 035204.

29.   R. Soref In *Group IV photonics for the mid infrared*, 2013; pp 862902-862902-15.

30.   Y. Masafumi, I. Ryo, I. Yuki, K. Sanghyeon, T. Hideki, Y. Tetsuji, Y. Hisashi, I. Osamu, F. Noboru, H. Masahiko, T. Mitsuru, T. Shinichi, *Semiconductor Science and Technology* **2013,** *28*, 094009.

31.   H. Kroemer, T.-Y. Liu, P. M. Petroff, *Journal of Crystal Growth* **1989,** *95*, 96-102.

32.   R. Soref, *Philosophical Transactions of the Royal Society of London A: Mathematical, Physical and Engineering Sciences* **2014,** *372*.

33.   N. Von Den Driesch, D. Stange, S. Wirths, G. Mussler, B. Holländer, Z. Ikonic, J. M. Hartmann, T. Stoica, S. Mantl, D. Grützmacher, D. Buca, *Chemistry of Materials* **2015,** *27*, 4693-4702.

34.   S. Gupta. Germanium-tin (GeSn) technology. Stanford University, 2013.

35.   R. Chen, S. Gupta, Y.-C. Huang, Y. Huo, C. W. Rudy, E. Sanchez, Y. Kim, T. I. Kamins, K. C. Saraswat, J. S. Harris, *Nano Letters* **2014,** *14*, 37-43.

36. H. Lin, R. Chen, W. Lu, Y. Huo, T. I. Kamins, J. S. Harris, *Applied Physics Letters* **2012,** *100*, 102109.

37. S. I. Shah, J. E. Greene, L. L. Abels, Q. Yao, P. M. Raccah, *Journal of Crystal Growth* **1987,** *83*, 3-10.

38. S. Wirths, Z. Ikonic, A. T. Tiedemann, B. Holländer, T. Stoica, G. Mussler, U. Breuer, J. M. Hartmann, A. Benedetti, S. Chiussi, D. Grützmacher, S. Mantl, D. Buca, *Applied Physics Letters* **2013,** *103*, 192110.

39. A. B. Talochkin, V. I. Mashanov, *Applied Physics Letters* **2014,** *105*, 263101.

40. R. Chen, H. Lin, Y. Huo, C. Hitzman, T. I. Kamins, J. S. Harris, *Applied Physics Letters* **2011,** *99*, 181125.

41. S. Takeuchi, A. Sakai, O. Nakatsuka, M. Ogawa, S. Zaima, *Thin Solid Films* **2008,** *517*, 159-162.

42. R. Chen, Y.-C. Huang, S. Gupta, A. C. Lin, E. Sanchez, Y. Kim, K. C. Saraswat, T. I. Kamins, J. S. Harris, *Journal of Crystal Growth* **2013,** *365*, 29-34.

43. S. Barth, F. Hernandez-Ramirez, J. D. Holmes, A. Romano-Rodriguez, *Progress in Materials Science* **2010,** *55*, 563-627.

44. S. Barth, R. Jimenez-Diaz, J. Samà, J. D. Prades, I. Gracia, J. Santander, C. Cane, A. Romano-Rodriguez, *Chemical Communications* **2012,** *48*, 4734-4736.

45. G. W. Sears, *Acta Metallurgica* **1955,** *3*, 361-366.

46. S. A. Morin, S. Jin, *Nano Letters* **2010,** *10*, 3459-3463.

47. K. L. Choy, *Progress in Materials Science* **2003,** *48*, 57-170.

48. M. T. Borgstrom, G. Immink, B. Ketelaars, R. Algra, P. a. M. Bakkerserik, *Nat Nano* **2007,** *2*, 541-544.

49. R. S. Wagner, W. C. Ellis, *Applied Physics Letters* **1964,** *4*, 89-90.

50. M. Bar-Sadan, J. Barthel, H. Shtrikman, L. Houben, *Nano Letters* **2012,** *12*, 2352-2356.

51. J. E. Allen, E. R. Hemesath, D. E. Perea, J. L. Lensch-Falk, Liz.Y, F. Yin, M. H. Gass, P. Wang, A. L. Bleloch, R. E. Palmer, L. J. Lauhon, *Nat Nano* **2008,** *3*, 168-173.

52. S. Barth, M. S. Seifner, J. Bernardi, *Journal of Materials Chemistry C* **2014,** *2*, 5747-5751.

53. S. Barth, M. M. Koleśnik, K. Donegan, V. Krstić, J. D. Holmes, *Chemistry of Materials* **2011,** *23*, 3335-3340.

54. T. J. Trentler, K. M. Hickman, S. C. Goel, A. M. Viano, P. C. Gibbons, W. E. Buhro, *Science* **1995,** *270*, 1791-1794.

55. J. D. Holmes, K. P. Johnston, R. C. Doty, B. A. Korgel, *Science* **2000,** *287*, 1471.

56.   A. T. Heitsch, D. D. Fanfair, H.-Y. Tuan, B. A. Korgel, *Journal of the American Chemical Society* **2008,** *130*, 5436-5437.

57.   F. Wang, A. Dong, J. Sun, R. Tang, H. Yu, W. E. Buhro, *Inorganic Chemistry* **2006,** *45*, 7511-7521.

58.   X. Lu, B. A. Korgel, *Chemistry – A European Journal* **2014,** *20*, 5874-5879.

59.   X. Lu, C. M. Hessel, Y. Yu, T. D. Bogart, B. A. Korgel, *Nano Letters* **2013,** *13*, 3101-3105.

60.   A. T. Heitsch, C. M. Hessel, V. A. Akhavan, B. A. Korgel, *Nano Letters* **2009,** *9*, 3042-3047.

61.   R. Laocharoensuk, K. Palaniappan, N. A. Smith, R. M. Dickerson, D. J. Werder, J. K. Baldwin, J. A. Hollingsworth, *Nat Nano* **2013,** *8*, 660-666.

62.   T. Hanrath, B. A. Korgel, *Journal of the American Chemical Society* **2002,** *124*, 1424-1429.

63.   J. S. Kulkarni, O. Kazakova, J. D. Holmes, *Applied Physics A* **2006,** *85*, 277-286.

64.   H.-Y. Tuan, D. C. Lee, T. Hanrath, B. A. Korgel, *Chemistry of Materials* **2005,** *17*, 5705-5711.

65.   Y.-J. Zhu, F. Chen, *Chemical Reviews* **2014,** *114*, 6462-6555.

66.   C. Gabriel, S. Gabriel, E. H. Grant, E. H. Grant, B. S. J. Halstead, D. Michael P. Mingos, *Chem Soc Rev* **1998,** *27*, 213-224.

67.   J.-S. Schanche, *Molecular Diversity* **2003,** *7*, 291-298.

68.   S. H. Jhung, T. Jin, Y. K. Hwang, J.-S. Chang, *Chemistry – A European Journal* **2007,** *13*, 4410-4417.

69.   R. N. Gedye, F. E. Smith, K. C. Westaway, *Canadian Journal of Chemistry* **1988,** *66*, 17-26.

70.   R. N. Gedye, W. Rank, K. C. Westaway, *Canadian Journal of Chemistry* **1991,** *69*, 706-711.

71.   M. Nishioka, M. Miyakawa, H. Kataoka, H. Koda, K. Sato, T. M. Suzuki, *Nanoscale* **2011,** *3*, 2621-2626.

72.   S. Horikoshi, H. Abe, K. Torigoe, M. Abe, N. Serpone, *Nanoscale* **2010,** *2*, 1441-1447.

73.   M. Baghbanzadeh, L. Carbone, P. D. Cozzoli, C. O. Kappe, *Angewandte Chemie International Edition* **2011,** *50*, 11312-11359.

74.   M. A. Herrero, J. M. Kremsner, C. O. Kappe, *The Journal of Organic Chemistry* **2008,** *73*, 36-47.

75.   D. Obermayer, B. Gutmann, C. O. Kappe, *Angewandte Chemie International Edition* **2009,** *48*, 8321-8324.

76.   B. Gutmann, D. Obermayer, B. Reichart, B. Prekodravac, M. Irfan, J. M. Kremsner, C. O. Kappe, *Chemistry-A European Journal* **2010,** *16*, 12182-12194.

77.   C. O. Kappe, *Chem Soc Rev* **2008,** *37*, 1127-1139.

78.   J. M. Kremsner, C. O. Kappe, *The Journal of Organic Chemistry* **2006,** *71*, 4651-4658.

79.   C. Boztug, J. R. Sánchez-Pérez, F. Cavallo, M. G. Lagally, R. Paiella, *ACS Nano* **2014,** *8*, 3136-3151.

80.   S. T. Picraux, S. Dayeh, P. Manandhar, D. Perea, S. Choi, *JOM* **2010,** *62*, 35-43.

81.   K. C. Saraswat, *ECS Transactions* **2010,** *33*, 101-108.

82.   R. L. Ruben, M. Tatsuro, J. Wipakorn, H. Hiroyuki, U. Noriyuki, M. Shu, T. Masatoshi, L. Jean-Pierre, *Applied Physics Express* **2013,** *6*, 101301.

83.   R. Soref, *Nat Photon* **2010,** *4*, 495-497.

84.   R. T. Beeler, J. Gallagher, C. Xu, L. Jiang, C. L. Senaratne, D. J. Smith, J. Menéndez, A. V. G. Chizmeshya, J. Kouvetakis, *ECS Journal of Solid State Science and Technology* **2013,** *2*, Q172-Q177.

85.   R. Roucka, J. Xie, J. Kouvetakis, J. Mathews, V. D'costa, J. Menendez, J. Tolle, S. Yu, *J. Vac. Sci. Technol. B* **2008,** *26*, 1952-1960.

86.   H. Gerung, S. D. Bunge, T. J. Boyle, C. J. Brinker, S. M. Han, *Chemical Communications* **2005**, 1914-1916.

87.   D. D. Vaughn, J. F. Bondi, R. E. Schaak, *Chemistry of Materials* **2010,** *22*, 6103-6108.

88.   D. C. Lee, J. M. Pietryga, I. Robel, D. J. Werder, R. D. Schaller, V. I. Klimov, *Journal of the American Chemical Society* **2009,** *131*, 3436-3437.

89.   S. C. Codoluto, W. J. Baumgardner, T. Hanrath, *CrystEngComm* **2010,** *12*, 2903-2909.

90.   N. Zaitseva, Z. R. Dai, C. D. Grant, J. Harper, C. Saw, *Chemistry of Materials* **2007,** *19*, 5174-5178.

91.   H. W. Chiu, S. M. Kauzlarich, *Chemistry of Materials* **2006,** *18*, 1023-1028.

92.   D. Carolan, H. Doyle, *Journal of Materials Chemistry C* **2014,** *2*, 3562-3568.

93.   S. Prabakar, A. Shiohara, S. Hanada, K. Fujioka, K. Yamamoto, R. D. Tilley, *Chemistry of Materials* **2010,** *22*, 482-486.

94.   M. Veith, M. Jarczyk, V. Huch, *Chemische Berichte* **1988,** *121*, 347-355.

95.   E. Muthuswamy, A. S. Iskandar, M. M. Amador, S. M. Kauzlarich, *Chemistry of Materials* **2013,** *25*, 1416-1422.

96.	H. Gerung, T. J. Boyle, L. J. Tribby, S. D. Bunge, C. J. Brinker, S. M. Han, *Journal of the American Chemical Society* **2006,** *128*, 5244-5250.

97.	R. J. A. Esteves, M. Q. Ho, I. U. Arachchige, *Chemistry of Materials* **2015,** *27*, 1559-1568.

98.	M. I. Bodnarchuk, K. V. Kravchyk, F. Krumeich, S. Wang, M. V. Kovalenko, *ACS Nano* **2014,** *8*, 2360-2368.

99.	D. J. Xue, J. J. Wang, Y. Q. Wang, S. Xin, Y. G. Guo, L. J. Wan, *Advanced Materials* **2011,** *23*, 3704-3707.

100.	M. Veith, *Chemical Reviews* **1990,** *90*, 3-16.

101.	M. Veith, M. Grosser, *Zeitschrift für Naturforschung B* **1982,** *37*, 1375-1381.

102.	M. Veith, M. Grosser, O. Recktenwald, *Journal of Organometallic Chemistry* **1981,** *216*, 27-38.

103.	M. Veith, M.-L. Sommer, D. Jäger, *Chemische Berichte* **1979,** *112*, 2581-2587.

104.	M. Dasog, J. G. C. Veinot, *physica status solidi (a)* **2012,** *209*, 1844-1846.

105.	G. B. De Los Reyes, M. Dasog, M. Na, L. V. Titova, J. G. C. Veinot, F. A. Hegmann, *Physical Chemistry Chemical Physics* **2015,** *17*, 30125-30133.

106.	S. A. Dayeh, J. Wang, N. Li, J. Y. Huang, A. V. Gin, S. T. Picraux, *Nano Letters* **2011,** *11*, 4200-4206.

107.	P. Madras, E. Dailey, J. Drucker, *Nano Letters* **2009,** *9*, 3826-3830.

108.	D. C. Bell, Y. Wu, C. J. Barrelet, S. Gradecak, J. Xiang, B. P. Timko, C. M. Lieber, *Microsc Res Tech* **2004,** *64*, 373-89.

109.	S. F. Li, M. R. Bauer, J. Menéndez, J. Kouvetakis, *Applied Physics Letters* **2004,** *84*, 867-869.

110.	H. Rücker, M. Methfessel, *Physical Review B* **1995,** *52*, 11059.

111.	M. Meléndez-Lira, J. Menéndez, W. Windl, O. Sankey, G. Spencer, S. Sego, R. Culbertson, A. Bair, *Physical Review B* **1996,** *54*, 12866.

112.	J. Menéndez, A. Pinczuk, J. Bevk, J. Mannaerts, *Journal of Vacuum Science & Technology B* **1988,** *6*, 1306-1309.

113.	J. Menendez, K. Sinha, H. Höchst, M. Engelhardt, *Applied Physics Letters* **1990,** *57*, 380-382.

114.	J. Groenen, R. Carles, G. Landa, C. Guerret-Piécourt, C. Fontaine, M. Gendry, *Physical Review B* **1998,** *58*, 10452.

115.	H. Lin, R. Chen, Y. Huo, T. I. Kamins, J. S. Harris, *Applied Physics Letters* **2011,** *98*, 261917.

116.	V. R. D'costa, J. Tolle, R. Roucka, C. D. Poweleit, J. Kouvetakis, J. Menéndez, *Solid State Communications* **2007,** *144*, 240-244.

117. A. Lugstein, M. Mijic, T. Burchhart, C. Zeiner, R. Langegger, M. Schneider, U. Schmid, E. Bertagnolli, *Nanotechnology* **2013,** *24*, 065701.

118. P. Aella, C. Cook, J. Tolle, S. Zollner, A. Chizmeshya, J. Kouvetakis, *Applied Physics Letters* **2004,** *84*, 888.

119. D. S. Sukhdeo, H. Lin, D. Nam, Z. Yuan, B. M. Vulovic, S. Gupta, J. S. Harris, B. Dutt, K. C. Saraswat In *Approaches for a viable germanium laser: tensile strain, GeSn alloys, and n-type doping*, 2013 Optical Interconnects Conference (IEEE, 2013), 2013; pp 112-113.

120. T. Fjeldberg, H. Hope, M. F. Lappert, P. P. Power, A. J. Thorne, *Journal of the Chemical Society, Chemical Communications* **1983**, 639-641.

121. R. G. Hobbs, S. Barth, N. Petkov, M. Zirngast, C. Marschner, M. A. Morris, J. D. Holmes, *Journal of the American Chemical Society* **2010,** *132*, 13742-13749.

122. A. Golloch, H. M. Kuß, P. Sartori, *Anorganisch-Chemische Präparate: Darstellung und Charakterisierung ausgewählter Verbindungen*. Walter de Gruyter: 1985.

123. C. A. Roskamp, E. J. Roskamp, *e-EROS Encyclopedia of Reagents for Organic Synthesis*.

124. M. F. Lappert, P. P. Power In *Di-and Trivalent Trimethylsilyl-Substituted Tin Amides and Related Compounds Such as Sn [N (SiMe3) 2] 2 or 3*, Organotin Compounds: New Chemistry and Applications: a Symposium, American Chemical Society: 1976; p 70.